MSc thesis

Permeability of simulated anhydrite fault gouge meter-scale samples in a dynamic flow-through system, combined with static batch experiments: implications for CO_2-rock interaction

Chris Heerema

June 12, 2015

Supervisors:
prof. dr. C.J. Spiers (Utrecht University)
dr. C.J. Peach (Utrecht Univeristy)
drs. T.K.T. Wolterbeek (Utrecht University)

Collaborator:
dr. A.M.H. Pluymakers (University of Oslo)

Table of Contents

Abstract

Numerous geological reservoirs considered for CO_2 storage, both in the Netherlands and elsewhere, are topped by anhydrite caprock. Faults cross-cutting these formations may form potential pathways for CO_2 leakage, possibly affecting storage integrity. To confidently assess the impact of such faults, an understanding is required of how CO_2-induced chemical reactions, such as the potential transformation of anhydrite to calcite, affect fault permeability. Prior to this study no clear consensus existed on the extent to which acidic CO_2-saturated water promotes the transformation of anhydrite into calcite and whether buffer capacity is of importance in this transformation. In this context, the present study addresses the effects of acidic CO_2-saturated fluid and alkaline $NaHCO_3$ solution on the mineralogical and transport properties of simulated anhydrite fault rock. To this end, we performed batch reaction experiments (duration 9 to 65 days) and meter-scale reactive flow-through experiments, both conducted at 80°C and 10 MPa fluid pressure, simulating storage reservoir conditions at about 3 km depth. The batch experiments involving CO_2-saturated water showed only very minor calcite precipitation, which we attribute to dissolution of dolomite (impurity in the anhydrite sample material) and subsequent re-precipitation as calcite upon experimental depressurization and CO_2 degassing. This inference is supported by the fact that calcite precipitation was not detected in a similar batch reaction experiment performed using dolomite-free sample material. By contrast, extensive calcite precipitation was observed in batch experiments employing $NaHCO_3$ solution, indicating that alkalinity is required in order for the anhydrite to calcite transformation to occur. No microstructural or permeability changes were observed in meter-scale flow-through experiments employing CO_2-saturated deionized water. We therefore conclude that here is no risk of calcite formation in anhydrite bearing fault zones, due to the presence of CO_2-saturated water (pH=3-4), in the absence of alkaline buffering. However, in the flow-through experiment using 0.5 M $NaHCO_3$ solution, we observed a zoned and intensely calcified flow-path that penetrated two-thirds of a meter into the sample, in under 60h of flow-time. We suspect this flow-path to be a self-enhancing pathway, which allows reactive alkaline fluid penetration, coupled with positive feedback involving porosity and permeability increase. Our results imply that acidic CO_2-bearing pore fluid will not cause calcite formation and runaway porosity/permeability increase in faulted anhydrite caprock. However, if alkaline fluids penetrate faulted or fractured anhydrite caprock, localized calcification may severely alter transport and geomechanical characteristics of the fault or fracture system. We therefore express the need for caution if alkaline fluids are injected into a reservoir topped by anhydrite, which could the case in relation to carbon capture and storage combined with alkaline waste disposal or alkaline enhanced oil recovery.

1. Introduction

Capture and geological storage of CO_2 (CCS) in depleted oil and gas reservoirs is considered to be among the main options of reducing atmospheric CO_2 concentrations in the near future (Bachu, 2000; Scott et al., 2013). Structural and stratigraphic trapping of CO_2 therefore are among the prime methods of geological storage, and integrity of these structures has to be kept intact in order for CCS to be effective. Caprock crosscutting faults are among the most likely escape routes for supercritical (sc) CO_2 (Figure 1), since these faults may dilate during reactivation, which will increase porosity and permeability and potentially allow CO_2 outflow. As CO_2 might react with the fault rock, it is crucial to achieve good understanding of the spatial chemical interactions over time, in such faulted or fractured rock formations, in order for long-term CCS to be effective (Rochelle et al., 1999).

Many potential storage sites worldwide are capped by an anhydrite seal, including numerous near depleted and empty hydrocarbon fields in the Netherlands and the North Sea. And in addition, several pilot sites that are currently being utilized for CCS are also capped by anhydrite, for example the K-12B field, the Netherlands (van der Meer and van Wees, 2006) and the Weyburn and Zama fields, Canada (Li et al., 2005). In addition, anhydrite-bearing faults and CO_2 bearing fluids are associated with seismic activities in the Apennines, Central Italy. In the Apennines, Triassic Evaporites (e.g. anhydrites and dolomites) are identified as being the source region for strong earthquakes up to M~6 (Collettini et al., 2009; De Paola et al., 2008).

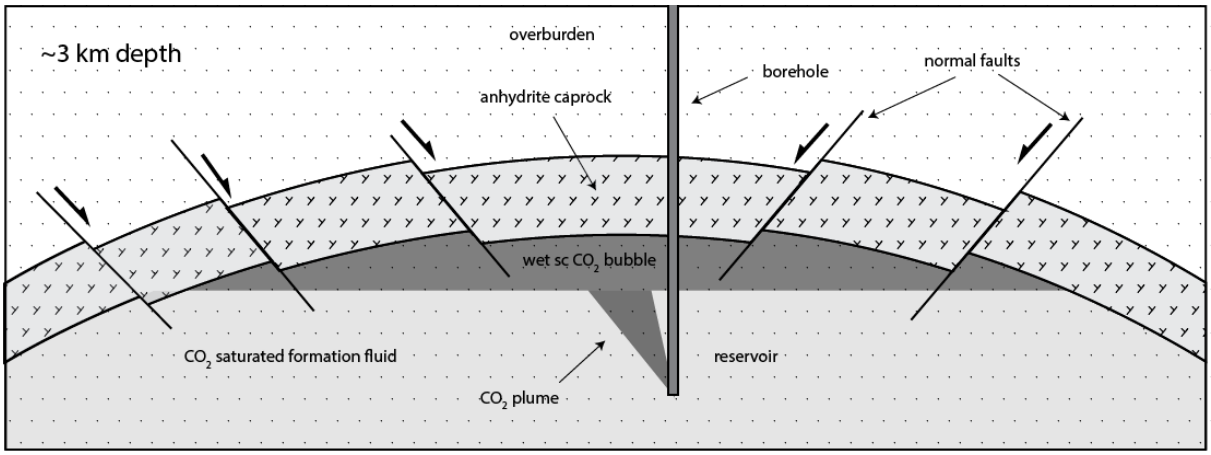

Figure 1 *Schematic diagram depicting various elements of a suggested CCS system during and after the injection of* CO_2*. This system is closed and therefore it is assumed that the formation fluid will stay in place. Modified after Rochelle et al. (2004).*

In an aquifer or hydrocarbon reservoir that has become recharged with brine after exploration, injected sc CO_2 will rise up as a plume and form a bubble at the top of the trap structure, which is overlain by the caprock (Johnson et al., 2004)(Figure 1). This bubble becomes water saturated over time, and the formation brine located below the CO_2 bubble will become saturated with CO_2 (King et al., 1992) (Figure 1). Injected CO_2 will dissociate and react with formation water and decrease pH to around 3-4 regardless of the rock formation (Luquot and Gouze, 2009) via the following reaction

$$CO_2 + H_2O \Leftrightarrow H_2CO_3 \Leftrightarrow HCO_3^- + H^+ \Leftrightarrow CO_3^{2-} + 2H^+ \quad \text{(R1)}$$

In wet anhydrite fault rock it may be expected that some anhydrite will dissolve (Figure 1) and will saturate the formation fluid with respect to Ca^{2+} and SO_4^{2-} ions through

$$CaSO_4 \Leftrightarrow Ca^{2+} + SO_4^{2-} \quad \text{(R2)}$$

This in turn implies that if dissolved CO_2 is present, calcite may form through:

$$Ca^{2+} + SO_4^{2-} + H_2CO_3 \Leftrightarrow CaCO_3 + 2H^+ + SO_4^{2-} \quad \text{(R3)}$$

There is no clear consensus on the conditions under which reaction (R3) is viable. On the one hand, experimental work suggests that reaction (R3) is viable in an acid environment (e.g. CCS system). For example, when brought in contact with CO_2-saturated water for 88h, Pluymakers et al. (2014) reported a doubling of the carbonate content (5 wt % to 11-16 wt %) by TGA analysis, in two separate compaction experiments using simulated anhydrite fault gouge. Also, Czernichowski-Lauriol et al. (1996) and Pearce et al. (1996) investigated the influence of CO_2-saturated fluids on anhydrite caprock in up to 8 month long batch experiments, in which they observed secondary calcite precipitation. They speculate that presence of CO_2 might favor calcite precipitation from Ca^{2+} ions released into solution. These findings indicate that calcite formation possibly occurs when anhydrite is brought into contact with CO_2-saturated water.

On the other hand, Kuhn et al. (2009) report that alkalinity or buffer capacity is of the utmost importance to shift reaction (R3) to the right, because at high pCO_2, carbonic acid (H_2CO_3) controls the acidity and thus the solubility of carbonate minerals (Garcia-Rios et al., 2014). Alkalinity is reported to neutralize the excess acid formed in reaction (R3) and favor calcite precipitation. In addition, geochemical modelling performed by Kuhn et al. (2009) demonstrates that reaction (R3) proceeds at pH higher than 5.5 (Figure 2), which they also verified by conducting batch experiments with anhydrite and an alkaline fluid ($NaHCO_3$), resulting in 92% calcification in fewer than 24h. This implies that acid CO_2-saturated formation water (pH=3-4) will not react with anhydrite to form calcite, unless an alkaline source is present. Alkalinity could be provided through feldspar weathering (Kuhn et al., 2009) in a natural system and through the injection of alkaline fluids in the light of, for example, alkaline enhanced oil recovery (EOR) (Lorenz and Peru, 1989) or alkaline waste disposal combined with CCS (Bobicki et al., 2012).

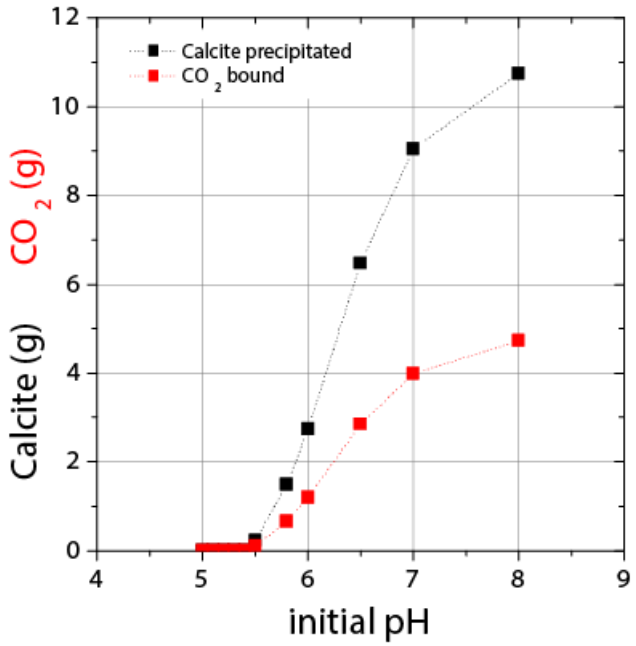

Figure 2 *Calcite and CO_2 bound versus initial pH of the pore fluid as modelled with PHREEQC; boundary conditions: mass of solution = 1kg, 0.16M $NaHCO_3$ solution, infinite amount of anhydrite, T = 30 °C, pCO_2 = 1 MPa. After Kuhn et al. (2009).*

In addition to reaction viability, there is a need to investigate the potential reaction effects on fault permeability. $CaSO_4$ and $CaCO_3$ differ in molar volume, being 46.1 cm^3/mole and 36.9 cm^3/mole respectively. So the transition of anhydrite into calcite would yield a 20% net volume loss per mole and thus may results in porosity increase (Kuhn et al., 2009) and possibly permeability increase as well. Furthermore, flow-through experiments using cm-sized anhydrite cemented cores and sodiumcarbonate (Na_2CO_3) solutions demonstrate permeability doubling (Kuhn et al., 2009), while other similar experiments, also using Na_2CO_3 and anhydrite cemented sandstone cores, reveal no permeability change (Kazempour et al., 2012). However, all mentioned experiments are performed on cm-scale core samples. Geological faults cross-cutting the caprock are expected to be 10's to 100's of meters long, and on this larger length-scale it might be possible to have dissolution in the first part, and calcite precipitation occurring further along the fault. If precipitation of calcite then concentrates at the necks of the pores, a permeability decrease might be observed (Armitage et al., 2013).

There thus is a clear need for further research regarding the anhydrite-calcite transformation. Therefore, we will report the results of batch experiments on several combinations of simulated anhydrite fault gouge and CO_2-saturated water or $NaHCO_3$ solution. We added K-feldspar to some experiments to function as a low-alkaline source, as Kuhn et al. (2009) emphasize that the formation of a secondary silicate phase (e.g. illite, kaolinite) due to feldspar weathering is a possibility for binding CO_2. Also, length-scale is always an issue in experimental research. Therefore, this paper strongly distinguishes itself from previous research on cm-scale samples and will assess the chemical alteration of the anhydrite-calcite-CO_2 system on meter-scale. We will conduct meter-scale flow-through experiments using similar material and fluids as in our batch experiments. Through this we will assess the effects on permeability of long-range chemical and microstructural changes on simulated anhydrite fault gouge. Both types of experiments were conducted at a temperature of 80 °C (±0.1 °C) and at fluid pressures of 10 MPa, to represent in-situ conditions at around 3 km depth. We will place our results in a framework of existing literature and previous work, of which the implications are directly relevant to CCS, alkaline fluid injection (e.g. EOR, waste disposal) and anhydrite-bearing seismic terranes.

2. Methods

In this study, we test the effect of CO_2-saturated water and $NaHCO_3$ solutions on simulated anhydrite fault gouge at a typical reservoir temperature of 80°C and fluid pressures of around 10 MPa. We performed two types of experiments: batch experiments and meter-scale flow-through experiments. Our batch reaction experiments were conducted in order to test long-term effects of different pore fluids and to assess the viability of carbonate-forming reaction (R3). Our second type of experiments, meter-scale flow-through experiments, was conducted to assess any length-scale effects on anhydrite fault rock. Meter-scale samples were prepared by filling a stainless steel tube with crushed anhydrite, which was coiled after. This provides a compact manner to test the meter-scale spatial chemical interactions. In addition, the flow-through experiments allow for fluid refreshment, through which we reduce sample degassing, which could possibly cause mineral precipitation. This effect could not be reduced in our batch experiments, which were all degassed. All batch experiments are listed in Table 1 and all flow-through experiments in Table 2. Also, we did some preliminary geochemical modelling in order to comment on previous work done on this matter.

2.1 Sample material and pore fluids

The anhydrite rock used in this study was acquired from core material from the Hoogeweg-1 Well (Overijssel, The Netherlands), courtesy of Shell International Exploration and Production (SIEP) and the Nederlandse Aardolie Maatschappij (NAM). The core material was retrieved from the Zechstein 1 anhydrite member, which is located at the base of the Permian Zechstein evaporite formation (depth = 3200m) (Geluk, 2007). This borehole material contains about 3-6 wt% natural carbonates, determined to be dolomite through XRD analysis, and quantified using TGA. Using a pestle and mortar, we crushed and sieved the material to obtain the fraction with a grain size *d* between 50 µm and 212 µm. To reduce sample heterogeneities, all the sieved material was collected in one batch and thoroughly mixed. We describe the starting material in detail through grain size distribution and microstructural analysis. Four different starting materials were used in our experiments, which all consist mainly out of anhydrite, with minor to major chemical differences. To several experiments (Table 1 and 2) we added K-feldspar (Feldspar FS 900 S), commercially obtained from Amberger Kaolinwerke.

The used starting materials are listed below and briefly described:

I. Anhydrite α: initial carbonate content of 2.7 wt% (±0.5 wt%) (only used in Coil-A, Table 1).
II. Anhydrite β: initial carbonate content of 5.6 wt% (±0.5 wt%).
III. Anhydrite γ: consists of Anhydrite β to which 25 wt% K-feldspar was added, to induce more chemical reaction. It has 4.0 wt% (±0.5 wt%) initial carbonate content.
IV. Anhydrite δ: was treated with acid, resulting in 0 wt% initial carbonate content, to provide a method to solely look at chemical effects on anhydrite.

The starting materials were stored in a low humidity (<30%) environment, to avoid rehydration of sample material to gypsum, which occurs at temperatures below 65°C (Charola et al., 2007). Due to various reasons the sample material sometimes was in contact with water at low temperatures (<60°C) for several hours. We performed control experiments to determine the rate of rehydration, which showed that up to three days of rehydration time at ambient conditions led to no detectable gypsum content in the crushed and sieved material (tested by TGA, detection limit >0.25%)

The acid-treated starting material (anhydrite δ (Table 1)) was prepared by leaving 50 g anhydrite β to react with 200 ml 3M HCl over the weekend, ensuring that all carbonates will be dissolved. The acid-treated material was thoroughly washed with deionized water after and stored as previously described. We did not perform microstructural analysis on this material before or after experimentation.

We prepared $NaHCO_3$ solutions by adding 1 liter deionized water to 42 g or 13.5 g of fine $NaHCO_3$ powder, in order to make solutions of composition 0.5 M and 0.16 M respectively. These solutions were thoroughly mixed and left to equilibrate at ambient conditions for at least a day. CO_2-saturated pore fluid preparation for both types of experiments is described in following sections.

Experiment	Starting Material	Degassing (y/n)	$P_f/_PCO_2$ (MPa)	Pore fluid	Calcite formation (XRD)	Final carbonate content (wt% by TGA)	Total reaction time	Amount of material	Pore fluid volume (ml)
Batch 1	β	yes	10	CO_2 sat. water	yes	5.4	21 days	10 g	30
Batch 2	β	yes	10	CO_2 sat. water	yes	5.6	65 days	10 g	15
Batch 3	β	Yes	10	CO_2 sat. water	yes	4.8	21 days	10 g	15
Batch 4	γ	yes	10	CO_2 sat. water	yes	4.0	21 days	10 g	15
Batch 5	δ	yes	10	CO_2 sat. water	no	0	40 days	5 g	15
Batch 6	β	yes	10	0.16 M $NaHCO_3$	yes	6.8	9 days	10 g	15
Batch 7	β	yes	10	0.5 M $NaHCO_3$	yes	10.8	17 days	5 g	15

Table 1 *Performed batch reaction experiments. $P_f/_PCO_2$ is the pressure of the system to which the CO_2 is saturated, total reaction time indicates for how long the batch reaction was run, pore-fluid volume is the amount of de-ionized water or $NaHCO_3$ solution present in the system.*

Experiment	Starting Material	Pore fluid	φ_0 (%)	P_f (MPa)	$_PCO_2$ (MPa)	κ_0 (m^2)	κ_{end} (m^2)	Calcite formation (y/n)	Reaction time (connected)	Reaction time (blocked-in)	Flow-through volume (ml)
Coil-A	α	CO_2 sat. water	42.5	10.0-10.2	9.8-9.9	-	-	No	11 days	33 days	200
Coil-B	γ	CO_2 sat. water	42	10.0-10.2	9.8-9.9	$5.8x10^{-12}$	$6.0x10^{-12}$	Yes	28 days	3 days	180
Coil-C	β	0.5 M $NaHCO_3$	37	10	-	$2.4x10^{-12}$	$4.5x10^{-12}$	Yes	0 days	12 days	540

Table 2 *Summary of the experimental conditions of the meter-scale samples. ϕ_0 denotes the initial porosity of the material inside the tube, P_f the pore fluid pressure, $_PCO_2$ denotes applied CO_2 pressure at which the pore fluid is equilibrated, κ_0 the initial permeability of the sample, κ_{end} the final permeability of the sample, connected reaction time indicates the accumulated time at which the sample was left to equilibrate with the upstream pump, blocked-in reaction time is the duration at which the sample was closed off, flow-through volume is the total amount of CO_2-bearing fluid flowed through the system.*

2.2 Batch reaction experiments

These experiments were conducted in order to test long-term effects of CO_2 bearing fluids on the starting materials (Table 1), and to distinguish the effect of mineral precipitation due to CO_2 degassing. We used four Teflon-lined, stainless steel pressure vessels (volume = 61.5 ml), each equipped with an analogue pressure gauge. These pressure vessels were filled with 5-10g starting material, to which 15-30 ml of deionized and evacuated water or $NaHCO_3$ solution was added, submerging the sample (Table 3), and thirdly pressurized with sc CO_2. Subsequently the vessels were placed in a temperature controlling oil bath (80 °C (±0.1 °C)) and excess pressure due to heating was slowly bled off until a pressure of 10 MPa (± 0.3 MPa) was maintained. Vessels were then left for the desired amount of time (Table 1). Subsequently, over the course of reaction, pressure remained constant within 1 MPa. After the completion of an experiment, the vessel was allowed to slowly degas and depressurize for a day. Afterward the sample was removed from the oil bath and allowed to cool for several hours. After taking the assembly apart, the remaining sample was collected and thoroughly washed using deionized water, and oven dried (>65 °C) after. For post-experimental chemical analysis >3g of material was pulverized and mixed to be analyzed through X-ray Diffraction (XRD) and Thermogravimetric Analysis (TGA). XRD was used to qualitatively distinguish the different minerals (calcite, aragonite, dolomite, $NaHCO_3$), whereas TGA was used as a quantitative method to determine total calcite/dolomite content and possible $NaHCO_3$ content. Microstructural analysis was conducted by use of a tabletop Secondary Electron Microscope (SEM), by gluing material pin stubs using silver epoxy and platinum coating them afterwards.

2.3 Flow-through experiments on the meter-scale

2.3.1 Coiled sample preparation

To prepare meter-scale samples, we intermittently funneled and firmly tamped 6-7 ml of gouge into a vertically oriented 2m long stainless steel tube (inner diameter 8 mm). This caused initial compaction to an estimated porosity of 37-42% (Table 2). After filling the stainless steel casing with powder it was closed off and coiled. At both ends of the steel casing, two additional 5 cm steel tubes were attached, through a combination of Swagelok and Nova connections (Figure 3b). These were filled with >99 wt% pure quartz sand (Heksenberg formation, for detailed info see Brzesowsky et al. (2011)) to act as a filter, closed off by a stainless steel 100 µm mesh filter (Figure 3b).

2.3.2 Experimental set-up

The meter-scale coiled sample is placed horizontally in a temperature controlled silicone oil bath (80 °C (±0.1 °C)) between two Teledyne ISCO Model 65D pumps (Figure 3a). Also, the oil bath circulates heated silicone oil around both the pumps. A Type-K thermocouple located in between the upstream pump and coiled sample ensures similar temperatures (80 °C (±0.1 °C) for the heat wiring around the bare tubes (not depicted on Figure 3a,b). In-built Honeywell Model TJE pressure transducers (range 0-137.9 MPa, accuracy 0.1% of full scale) regulate the pore fluid pressure in either constant-pressure or constant flowrate mode.

A small pressure vessel/sampler (~11 ml) can be attached to the downstream pump (Figure 3a), for emptying and fluid analysis. Emptying at a low flowrate (100-180 ml/h) allows for pressurized sampling and thus prevents CO_2 degassing and mineral precipitation.

Post-experimentation of Coil-A it came to light that the ISCO pumps were prone to strong pressure drifts in a short amount of time (48h). This resulted in inaccurate permeability data, because the LabView logged pressures did not correspond with the actual pressures exerted by the pumps. For

this reason we implemented a Keller PD-33X differential pressure transducer (DPT) (range 0-3.5 MPa, accuracy 0.1 KPa) into the system. A system of tubes and taps allowed us to fully separate the DPT from the rest of the system. Through Control Center Series software we were now able to correctly and more accurately log the differential pressure applied between both pumps. By means of preliminary flow-through experiments we determined DPT data below 0.05 MPa differential pressure not to have a linear relationship with permeability, possibly due to issues related to a small background pressures present in the DPT and working with low pressures in general. Therefore we use flow-through events applying 0.2 MPa differential pressure before and after experimentation to define more reliable initial and final permeability.

Due to this inaccurate permeability data, we consider Coil-A as a reactive flow-through experiment, in which fluid was refreshed. Material was still exposed to CO_2-saturated water for prolonged amounts of time at a temperature of 80 °C and at a pressure of around 10 MPa. Nearly 200 ml CO_2-saturated water was flowed through the sample. Coil-B and C were run and evaluated using the more accurate DPT data.

2.3.3 Experimental procedure: coil flooding and initial water permeametry

Once the sample is placed in the oil bath, it is incorporated into the set-up (Figure 3a) and the majority of the air is removed from the sample by flushing it with deionized water and evacuating for 1 hour after. Both ISCO pumps are recalibrated/zeroed before each experiment and prior to each experiment a leak test was carried out using deionized water, which involves pressurizing and heating the system without pressure gradient or flow-through. In this way, all permeability data could be corrected for minor valve leakage using these predetermined leak calibrations.

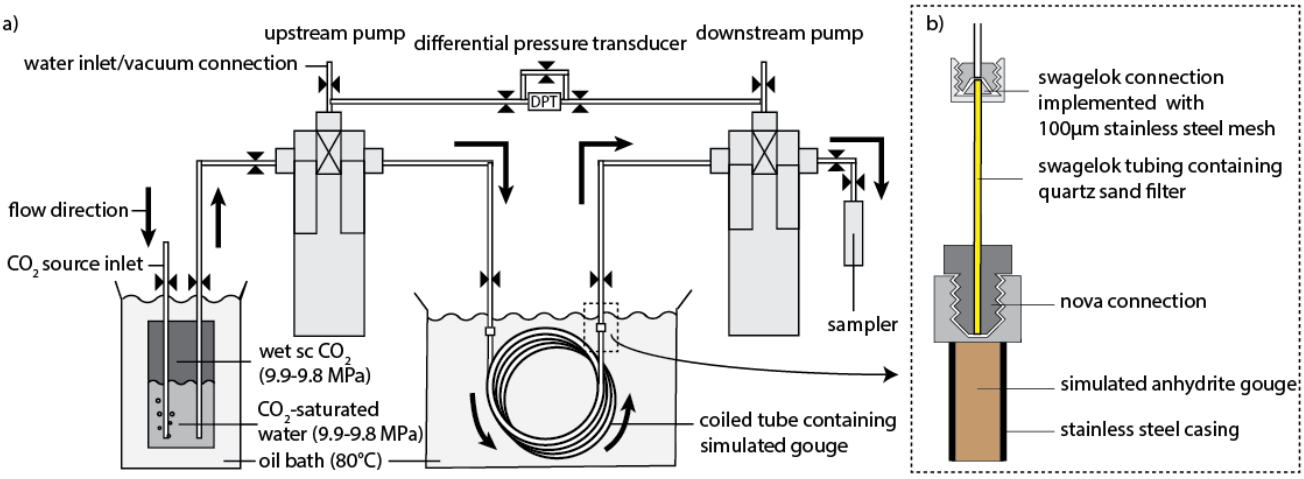

Figure 3 *a) Schematic figure of the experimental set-up and fluid flow through the CO_2 reactor vessel, upstream pump, sample, downstream pump and into the sampler. Insulation and heat wiring are not included in the drawing. b) Close-up of the coiled sample closing, including the quartz sand filter. Similar closing is found on the other end of the coil.*

All meter-scale flow-through experiments performed using CO_2-saturated water as pore fluid, were prepared as follows. This pore fluid was stored in a pressurized reactor vessel (~1l) containing both sc CO_2 and deionized water, which saturated each other at 9.8-9.9 MPa and 80 °C (±0.1 °C)(Figure 3a). Keeping the vessel pressurized just below 10 MPa ensures that no CO_2 degassing will occur during the experiments, preventing a two-phase flow and mineral precipitation. The reactor vessel is refilled with CO_2 using a Sprague pump when simultaneously CO_2-saturated water is provided to the upstream pump. During these events the pressure in the vessel is regulated, it has no external

pressure control. Refilling the vessel with deionized water was done through the connection with the upstream ISCO pump, during which slowly bleeding off excess CO_2 to the atmosphere maintained a near constant pressure. After each water refill of the vessel, the phases were given a week time to equilibrate.

Following the leak test, we measure the initial permeability of the samples, tested by pumping a minimum volume of 120 ml evacuated and de-ionized water through the sample, by opening connections on both sides of the sample (Figure 3a) and applying an approximate 0.2 MPa pressure difference. Furthermore, permeability was constantly measured during flow-through in either constant pressure or flowrate mode. And final permeability was once again measured using water and by applying a 0.2 MPa pressure difference. The apparent permeability of the set-up without sample presence was estimated at 10^{-10} m^2 (Wolterbeek, pers. comm., 2015).

2.3.4 Testing procedure using CO_2-saturated water or $NaHCO_3$ solution

After the initial water flow-through, the upstream pump was nearly filled with either CO_2-saturated water or $NaHCO_3$ solution (Table 2), allowing some space for thermal expansion. The fluid is allowed to warm up and equilibrate for 30 minutes. Flow-through is then initiated by opening the taps on both sides of the sample. Because of experimental procedure differences, we will describe the period between filling and emptying of the pumps for each meter- experiment separately.

Coil-A was run in constant-pressure mode. This involves applying 10.2 MPa (± 0.6 MPa) on the upstream pump and 10.0 MPa (± 0.6 MPa) on the downstream pump. Upon opening taps on both sides of the sample, flow ensues into the downstream pump. Due to technical issues, the experimental history of this sample is relatively complex. It involves several phases of cooling the sample to around 20°C (total time at room temperature <3 days). Furthermore, a very short phase of reversed flow was applied and two week periods of reaction time were applied, in which the upstream pump was left in open contact with the sample, keeping the downstream tap closed. This was imposed in order to allow the relatively large volume with CO_2-saturated fluid to diffuse into and possibly react with sample material. In all other instances the sample was shut-in on both sides.

Coil-B was also run in constant pressure mode, applying similar conditions as in Coil-A, with constant pressure difference measured by DPT to be 0.1-0.3 MPa. This experiment consists only of two consequent separate long-term reaction phases (17 and 11 days), in which there was an open connection with the upstream pump.

Coil-C was run in constant flowrate mode (10 ml/h), using $NaHCO_3$ solution. This involves pressurizing both pumps to 100 MPa (± 0.6 MPa), after which the taps on both sides of the sample are opened, subsequently the operating mode of the upstream pump was quickly switched to constant flow-rate at 10 ml/h. Once the flow-through of one pumpvolume is nearly completed, the sample gets blocked in again by closing the taps on both sides of the sample.

After flowthrough of a pumvolume, the upstream pump was refilled and the downstream pump was emptied using the sampler. During emptying of the pumps, two types of pore fluid samples were taken. First, pure fluid samples, without additives, were taken during water permeability tests. Second, the sampler was filled with 3 ml 1M HCl solution to prevent mineral precipitation during depressurization. These procedures can be repeated if necessary.

After finishing a meter-scale experiment the system is depressurized and the coil is extracted from the experimental apparatus to be prepared for microstructural and chemical analysis. It is oven dried for a week at 65 °C. Subsequently it is sawn into 5 cm segments, the sample is not completely dry yet at this moment. However, the remaining fluid coheres the material so it does not fall out when being

sawn, retaining the microstructure better. The cut parts are then labelled and tightly closed off at both ends with filter paper before left to dry again further.

2.3.5 Post experimental analysis

For post-experimental analysis, material was retrieved from the dry steel segments by carefully removing the filter paper and taking the required amount of powder. In Coil-A small amounts of powder (1-2 g) were retrieved for analysis, for Coil-B and C whole 5 cm sections were thoroughly mixed, and analyzed through TGA, XRD and Malvern Particle size analysis. Some powder or mm-sized clumps from selected steel segments were sprinkled on stubs and analyzed using the SEM.

Thick sections were created by putting a sawn 5 cm steel segment in a vertical position in a larger plastic container, flow-direction pointing up. The filter paper which covers the bottom end of the segment was punctured and the container filled with epoxy resin, enclosing the steel segment with resin, leaving the top in open connection with the air. Gravity and capillary forces then caused a large part of the 5 cm segment to fill with resin. Once dry, the impregnated sample was further sawn into thick-sections to be analyzed using light-reflectance microscopy (Leica DMRX).

The HCl diluted pore fluid samples were analyzed through Inductively Coupled Plasma Atomic Emission Spectroscopy (ICP-AES analysis) on selected ions.

2.3.6 Data processing

We logged pressure and volume data in all flow-through experiments at a frequency of 5 s using LabView based software and differential pressure data using Control Series 30 software. Darcy's equation (E1) allows calculation of effective permeability.

$$K = -\frac{Q \cdot \mu \cdot L}{(Pb - Pa) \cdot A} \qquad \text{(E1)}$$

Where K is the effective permeability (m^2), Q the total discharge (m^3/s), μ the dynamic viscosity (Pa·s), L the length of the sample (2m) over which the pressure difference (P_b-P_a) is active, A is the cross-sectional area (5.03×10^{-5} m^2) of the sample through which the flow occurs. Discharge, Q, is measured by dividing logged pumpvolume differences over a given time interval (5s). To obtain a representative value for viscosity of saturated solution, we used the quinary model of Li and Duan (2011) to calculate the speciation equilibration at 80 °C and 10.0 MPa. This model does not give information about the viscosity in this system. However, it does give the concentration of dissolved anhydrite at equilibrium. The ionic strength of this solution was converted to the molar equivalent of NaCl. Using the binary model, H_2O-NaCl, of Mao and Duan (2009) the viscosity was calculated at 3.58×10^{-4} Pa·s.

2.4 Geochemical modelling methods

Pluymakers and co-workers performed uni-axial compaction experiments on simulated anhydrite fault gouge (anhydrite α) at 80 °C and 15.3 MPa of fluid pressure, using pre-saturated $CaSO_4$ solution, pressurized with sc CO_2. They report a 10-15 wt% increase in carbonate content. This mechanical experiment can be considered a reaction experiment and we will use the quinary CO_2-H_2O-$CaCO_3$-$CaSO_4$-NaCl-system model of Li and Duan (2011) to simulate three end-member situations (ambient, heated, heated and pressurized) as described in the paper, to assess the effect of pressure, temperature and CO_2 degassing on $CaSO_4$ and $CaCO_3$ concentrations. According to the described experimental methods, 6.7 g of anhydrite α is loaded into the sample holder, and subsequently saturated with 3 ml $CaSO_4$-saturated water. The system is then heated, and subsequently pressurized

with sc CO_2. We will calculate the speciation equilibration of $CaCO_3$, $CaSO_4$ and CO_2 in g/l at ambient (T = 20 °C, $_PCO_2$ = 0.1 MPa), heated (T = 80 °C, $_PCO_2$ = 0.1 MPa), heated and pressurized (T = 80 °C, $_PCO_2$ = 15.3 MPa) conditions. Model parameters include excess amounts of $CaSO_4$ and $CaCO_3$ to represent the starting material. We use atmospheric CO_2 concentrations as input for ambient and heated conditions, because the system is then still in contact with the atmosphere. For the heated and pressurized conditions, we use an excess of CO_2. Furthermore, these simulations include an infinite amount of equilibration time.

3. Results and observations

3.1 Characterization of starting material

3.1.1 Particle size analysis

Using Malvern Particle sizes, we determined the initial grainsize distribution of the various starting materials; all three samples show relatively comparable curves (Figure 4). They all follow the same trend, no grains detected below 40 µm. The mode is around 110 µm and the largest grains are around 400 µm. Grains larger than the sieve mesh (> 212 µm) are present in the material, because the sieve filters the material based on the smallest diameter of a grain, whereas the Malvern Particle sizer optically analyses the largest diameter of a grain. Compared to anhydrite α, anhydrite β and γ have a slightly higher frequency of smaller grains (< 100 µm), while containing a lower frequency of larger grains (> 100 µm), though these differences are considered not to be significant.

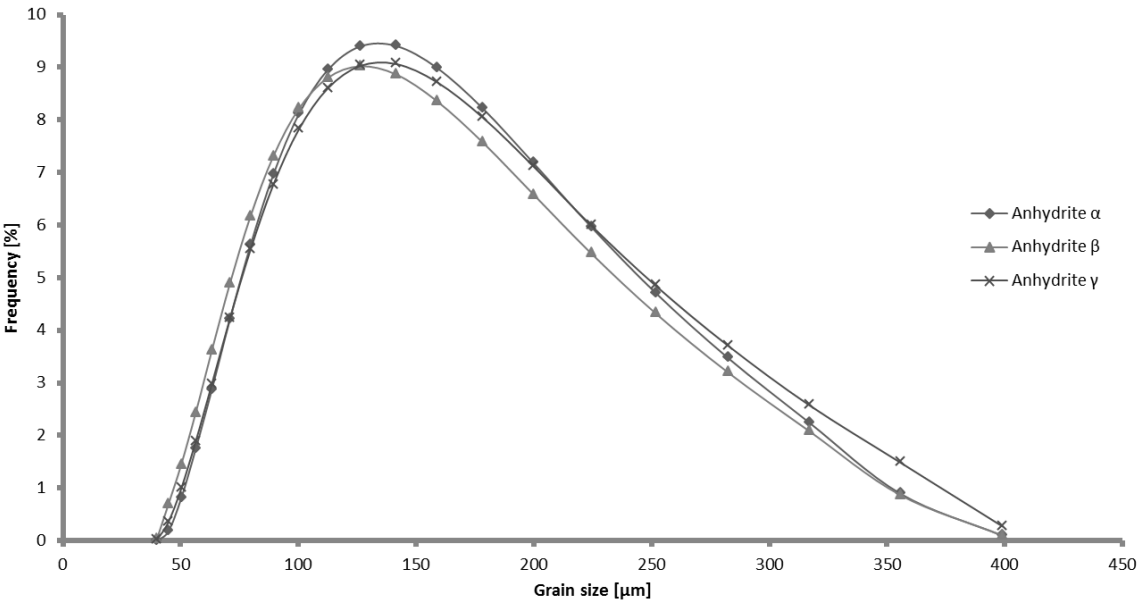

Figure 4 *Grainsize vs distribution frequency distribution of grain sizes used in the experiments. Data obtained using a Malvern Particle sizer.*

3.1.2 Microstructural analysis

An overview of the starting material is given in Figure 5a. This figure shows that grainsizes roughly correspond to sieve meshes (50-212 µm) and the particle size data (Figure 4). Zooming in on the individual anhydrite grains (Figure 5b) shows a blocky/angular shape, with sharp edges; the shape varies from low to high sphericity. The smooth fracture surface of the grains is dusted with very fine (<10 µm) material, which covers part of the surface of a grain. Dolomite grains can be optically distinguished from anhydrite by their rough surface and rounder edges (compare Figure 5c to Figure 5b). Also starting material with a number of feldspar grains is depicted (Figure 5d). On microscale level feldspar grains can be optically distinguished from anhydrite and dolomite, by their rougher surface and microporous structure.

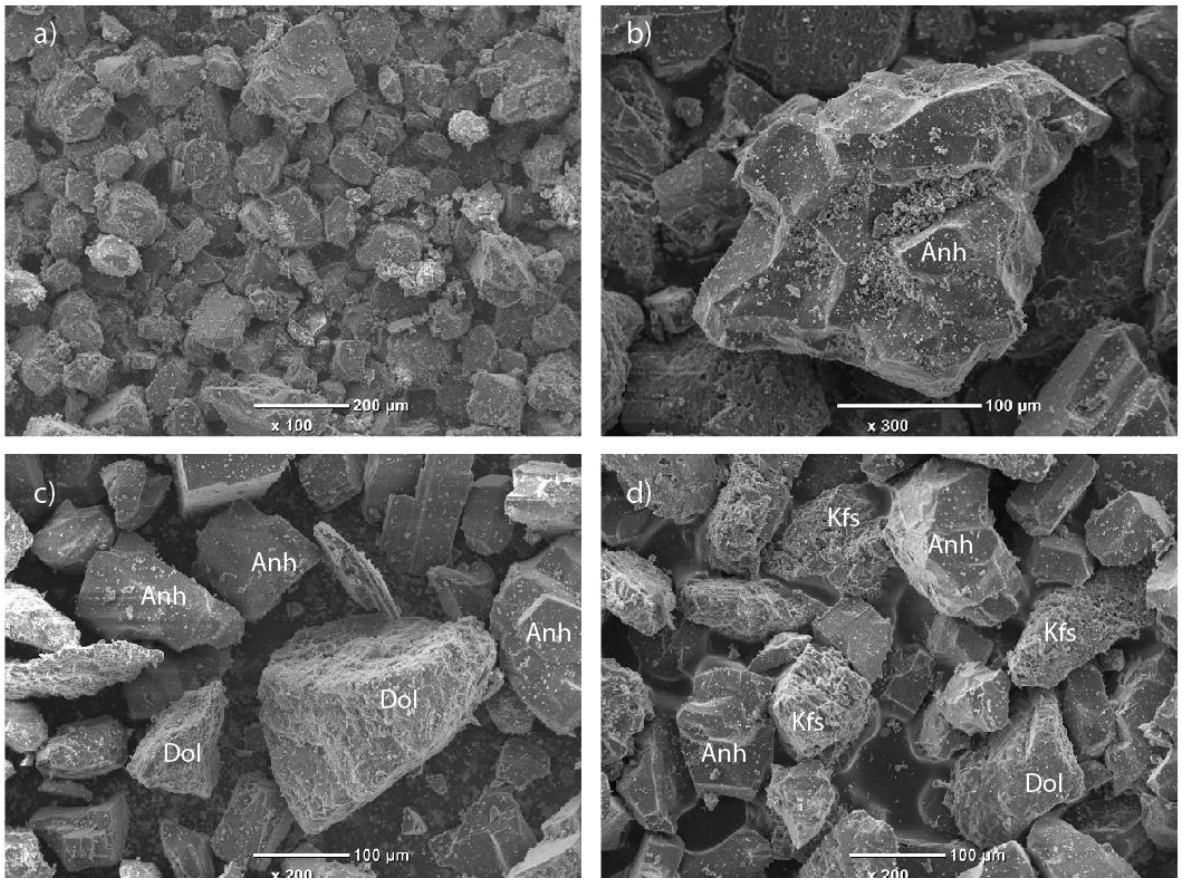

Figure 5 *Secondary electron images of the starting material. a) Overview of the starting material as used in the experiments. Only anhydrite grains are visible in this image. b) Focus on the microstructure of a single anhydrite grain, very fine grained material ("dust") accumulates in cavities. c) Distinct rough surface characteristics of dolomite grains. d)Three main minerals that are present in the starting material. K-feldspar is recognized by its microporous structure.*

3.2 Results of the batch reaction experiments

The overview and summary of the batch reaction results we conducted can be found in Table 1.

3.2.1 Chemical analysis

Three weeks to 2-month long batch experiments containing anhydrite β and CO_2-saturated water (Batch 1, 2 3, Table 1) all show calcite formation through qualitative XRD analysis. However, the final carbonate content analyzed quantitatively through TGA shows comparable values to the starting material (5.6 wt%), and even a slight decrease in Batch 3. Similar results were observed for the batch experiment using K-feldspar enriched starting material (Batch 4). The experiment using carbonate-free anhydrite (Batch 5, Table 1) demonstrates no carbonate detection through both XRD and TGA analysis after 40 days of reaction time. Three batch experiments containing 0.16 M and 0.5 M $NaHCO_3$ solution (Batch 6 and 7) all show calcite formation and an increase in carbonate content of around 2 and 6 wt% respectively (Table 1).

3.2.2 Microstructural analysis

Secondary electron images from Batch 1 and 4 show overall unaltered material (Figure 6a, c) compared to the starting material (Figure 5a-d). The material (Figure 6b,d) does appear to be less covered in fine –grained material with respect to the starting material (Figure 5a-d). Material from the other batch experiments with CO_2-saturated fluid gave similar results. We do not have a microstructural analysis of the alkaline reacted samples, but we assume similar observations as in our meter-scale alkaline sample (Section 3.3.4.2).

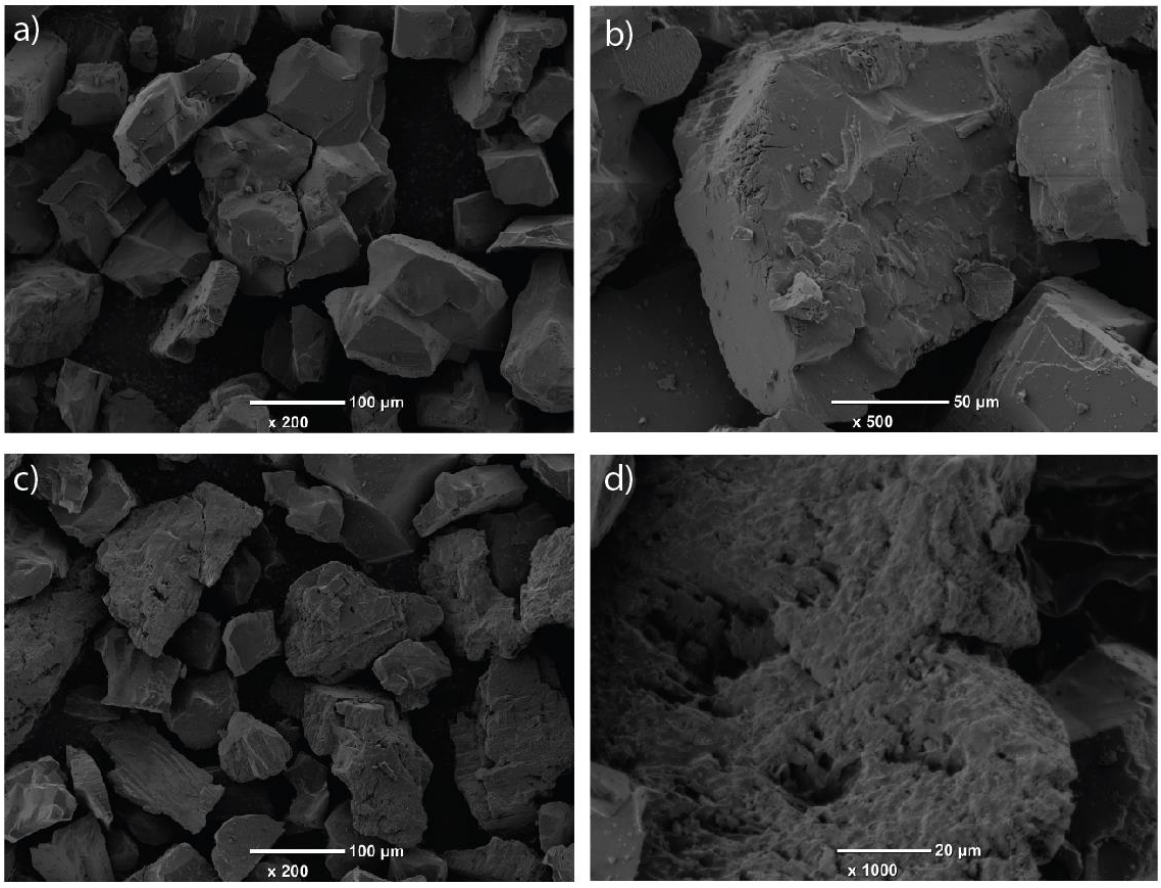

Figure 6 *Secondary electron images of Batch 1 and 4 after 21 days of reaction time. a) Overview of anhydrite grains (Batch 1). b) Zoom in on an anhydrite grain (Batch 1). c) Overview of K-feldspar and anhydrite grains (Batch 4). d) Zoom in on a single K-feldspar grain (Batch 4)*

3.3 Results of meter-scale flow-through samples

The summary and some results of the meter-scale flow-through experiments are listed in Table 2.

3.3.1 Chemical analysis of retrieved sample material

3.3.1.1 Experiments performed using CO_2-saturated water

The spatial carbonate distribution throughout Coil-A and B is shown in Figure 7a and 7b respectively. Variations of total carbonate content (TGA), through both meter-scale samples vary within a 1.5 wt% range. Measurements in Coil-A show a maximum 0.8 wt% increase or decrease from the starting material, no trends can be observed (Figure 7a), nor any calcite formation. In Coil-B, all values are either similar to or slightly above (+0.5 wt%) the base level, except for the first measurement (13 cm downstream) (Figure 7b). In addition at four locations calcite was detected through XRD analysis. Recall here that XRD is used as a qualitative method, to identify certain minerals, and that the measured concentrations only have an indicative meaning.

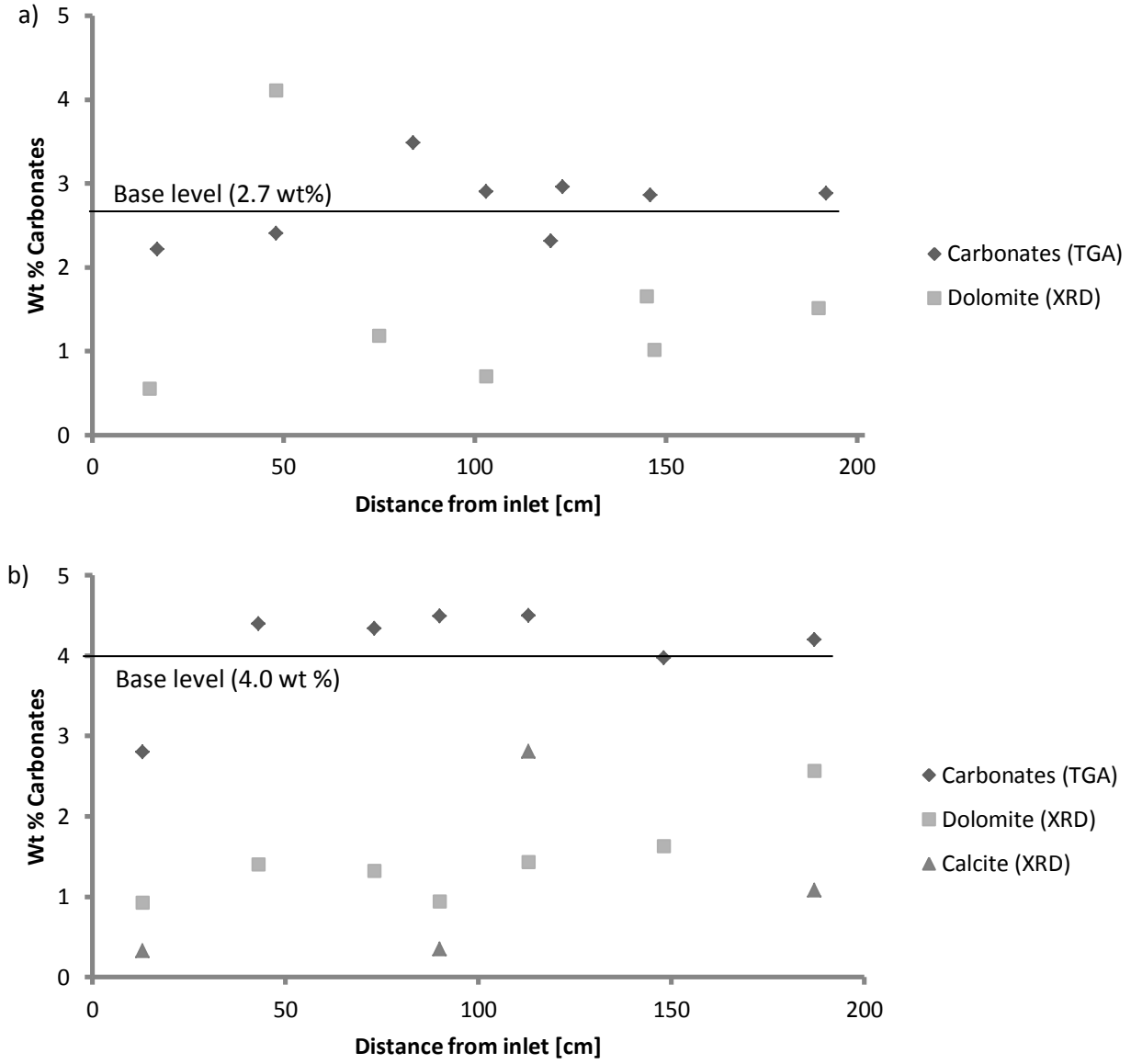

Figure 7 *Carbonate content distribution vs distance from inlet through Coil-A (a) Coil-B (b) determined by TGA (quantitative) and XRD analysis (qualitative).*

3.3.1.2 Experiments performed using 0.5 M $NaHCO_3$ solution

The analytical results for Coil-C, employing 0.5 M $NaHCO_3$ solution, show a significant increase in carbonate content at the beginning of the sample (67 wt %) (Figure 8). The graph consequently drops to 15 wt% carbonate content after which the curve shows several 5 wt % variations over a length of 40 cm, before reaching a minimum at around 75 cm. At this point no significant change is observed and a steady carbonate content of 6 wt% is maintained over the rest of the sample, which is 1-2 wt % over the initial carbonate content (Figure 8). This distribution was achieved in fewer than 60h of flow-time and a total of 540 ml pore fluid.

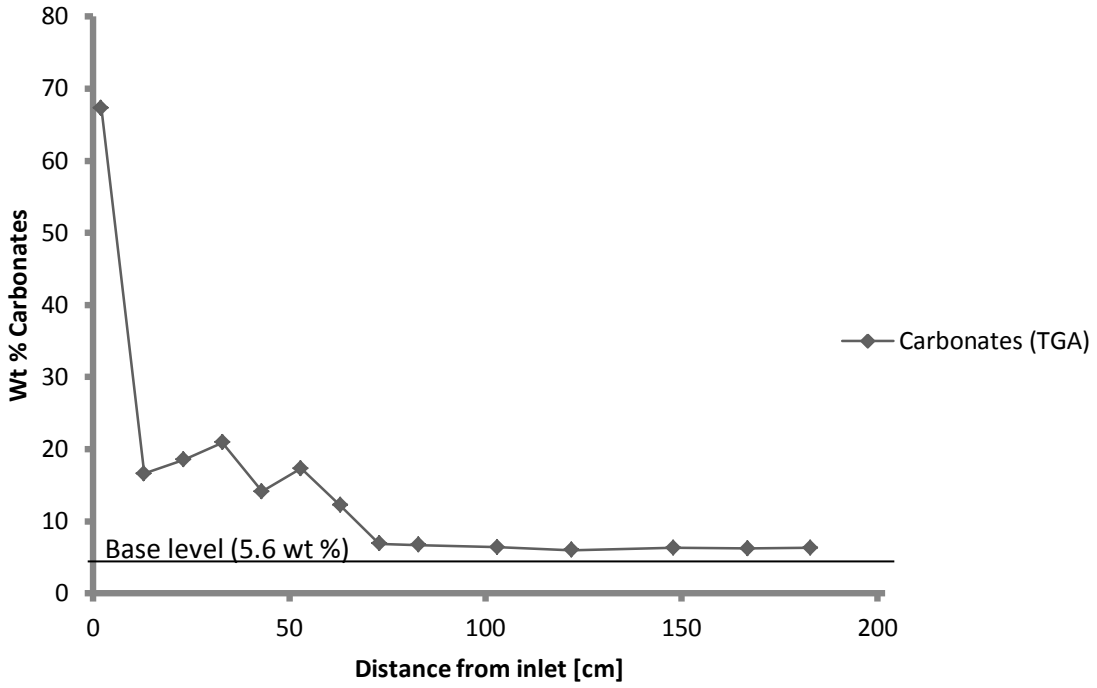

Figure 8 *Carbonate distribution vs distance from inlet of Coil-C is depicted. Base level indicates the initial carbonate content already present in starting material anhydrite* β*. Data acquired by TGA.*

3.3.2 Fluid analysis

3.3.2.1 Experiments performed using CO_2-saturated water

ICP-AES analysed fluids of Coil-A and B are presented in Figure 9a and 9b. Note that x-axis values do not represent a relative timescale, but the cumulative amount of days that the sample material was in contact with the pore fluid (CO_2-saturated fluid or water), after which it is sampled. For example the value 17 (Figure 9b) indicates that the fluid was analyzed after total sample contact time of 14 days. The calcium signal for all samples indicates high (500-700 ppm) concentrations. In the water samples, SO_4^{2-} concentrations roughly match the associated Ca-concentrations, while a larger offset is created in the CO_2-saturated samples for both coils (Figure 9a,b). Magnesium levels show generally higher concentrations in CO_2-saturated fluid samples (100 ppm) than in water samples (5 ppm for Coil-A (Figure 9a)). However, this is not the case in Coil-B, where Mg concentrations in all analyzed fluid samples vary around 20-50 ppm. Small amounts of potassium are present in all samples, with elevated concentrations observed in the (CO_2-saturated) fluid samples of Coil-B (Figure 9b) and aluminum concentrations do not exceed 8 ppm in all analyzed fluid samples.

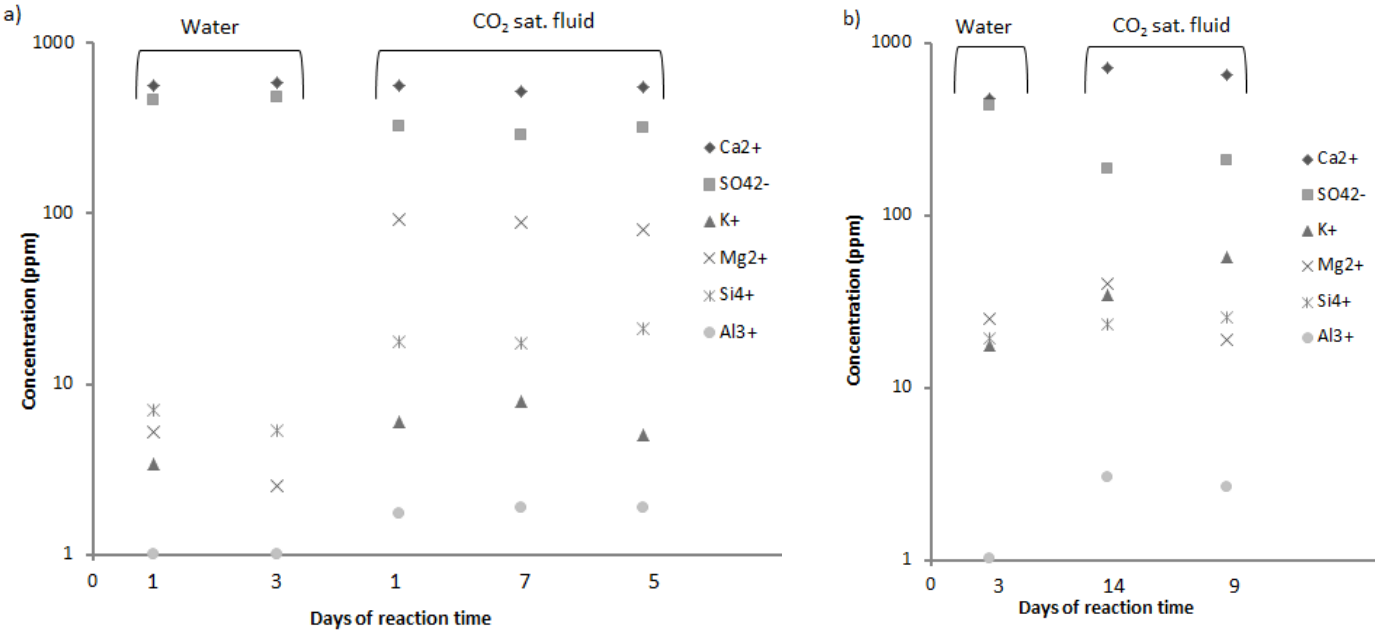

Figure 9 *ICP-AES analysis of the fluid of Coil-A (a) and Coil-B (b). Days of reaction time indicates the amount of time the sample material was in contact with the pore fluid, before it was sampled. Samples are presented in chronological order.*

3.3.3 Particle size analysis

We retrieved material from four intervals throughout Coil-A, showing overall comparable distribution frequency (Figure 10a), varying within 0.5% of each other. Particle size analysis however shows strong deviation from the starting material. Material retrieved from the sample with a grainsize ranging between 90 µm and 270 µm are all less frequent, while grains between 40 µm and 70 µm appear more frequent in the material retrieved from the sample, indicating a grainsize decrease.

For Coil-B we observed a trend with distance, where the positions further away from the inlet (113, 187 cm downstream) show near identical graphs, while the sample from 13 cm from the inlet shows an anomalously strong increase in fine grain sizes (Figure 10b). Another observation is the shift of the three later positions with respect of the starting material towards the right side of the spectrum. The largest grains measure up to 50 µm larger, the opposite is the case when comparing the starting material with the earlier position (13 cm). What also becomes evident from Coil-A and B is the increase in very fine material (< 30 µm) (Figure 10a,b), appearing as a small peak around the 15 µm grainsize. TGA analysis shows the material to have similar composition as the starting material.

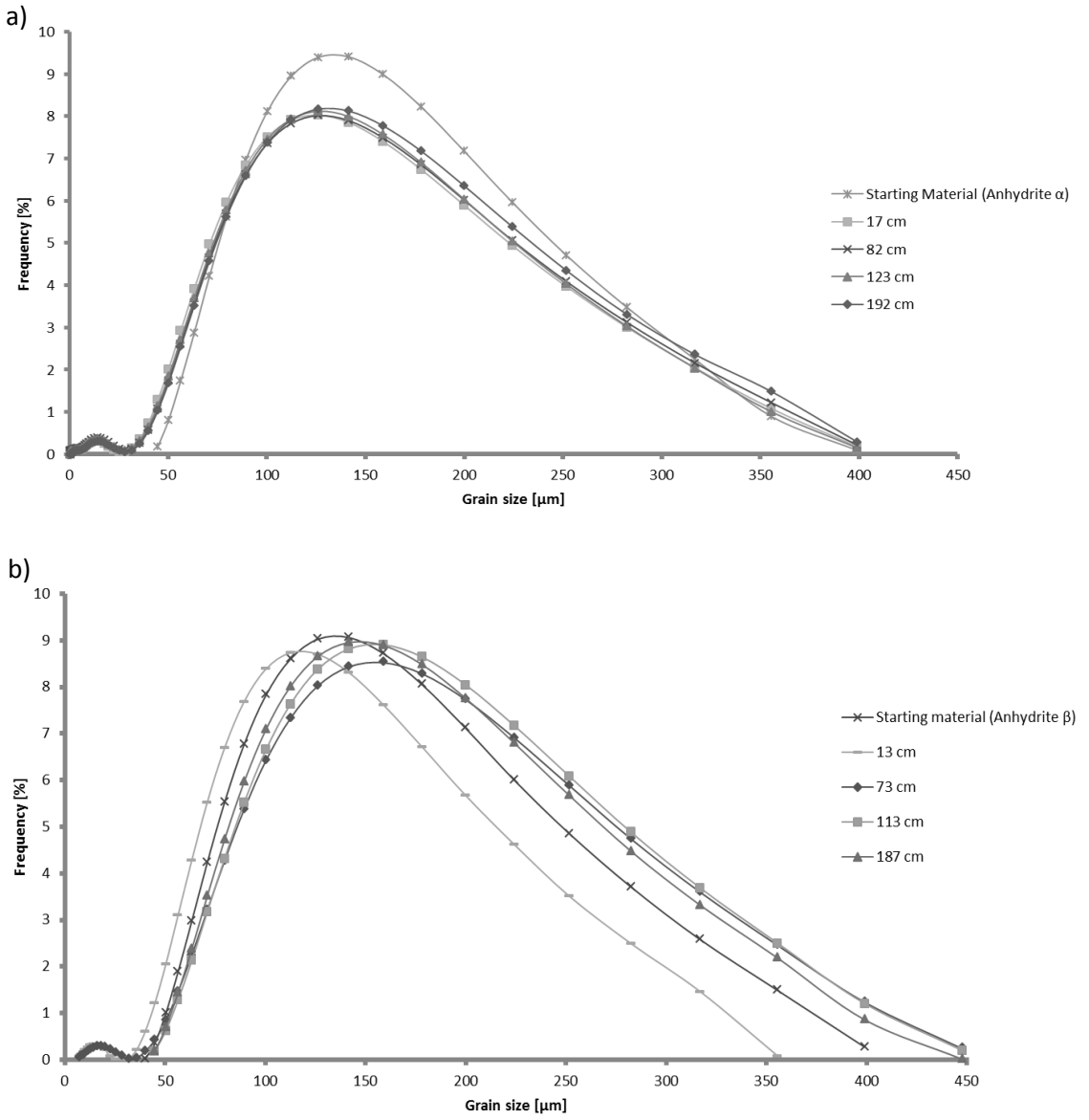

Figure 10 *Depicts the grain size vs distribution frequency at several intervals. a) Data obtained from Coil-A, at 17, 82, 123 and 192 cm downstream. b) Data obtained from Coil-B, at 13, 73, 113 and 187 cm downstream. Results obtained by Malvern Particle sizing.*

3.3.4 Microstructural analysis

3.3.4.1 Experiments performed using CO_2-saturated water

We retrieved generally incohesive material from both samples (Coil A and B). At certain points throughout the samples, some of the material was loosely clumped (mm sized) together, but disintegrated into loose powder when shaken gently, and was optically indistinguishable from the starting material. No trends with distance could be observed in both meter-scale samples; therefore the material characteristics described are representative per meter-scale samples (Coil-A and B).

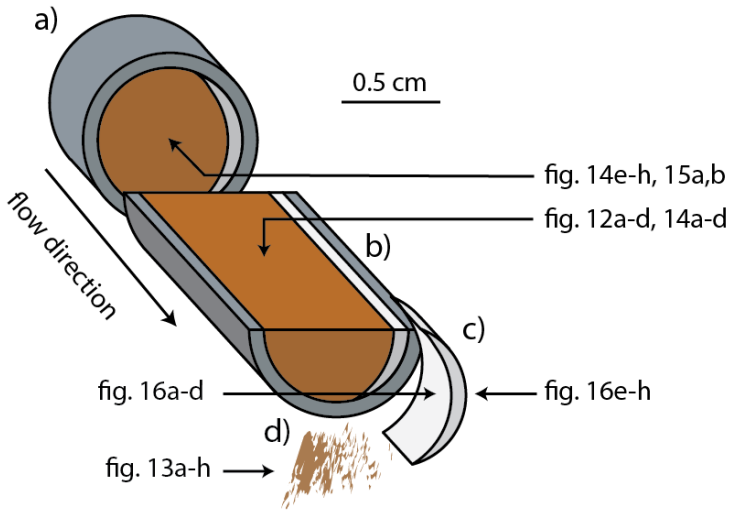

Figure 11 *Dissected steel segment for optical analysis, arrows indicate viewpoint per figure. a) Cross-section perpendicular to flow direction. Brown color indicates processed material. Grey crescent shape indicates coherent calcite scale (only found in Coil-C). b) Cross section parallel to flow direction. c) Separate extracted crescent shaped calcite scale (as found in Coil-C). d) Loose grains retrieved from a segment.*

We constructed a cartoon to clarify which cross sectional images correspond to which viewpoint (Fig. 11a-d). Cut and polished longitudinal cross sections of Coil-A and B are shown in Figure 12a and 12c respectively. In this cross-section Coil-A is heterogeneous in color, becoming lighter towards the top, whereas Coil-B is more homogeneously, and lighter, colored. Throughout both segments cavities, casing-material disconnections and lighter sections are observed. At the lower part of the segment from Coil-A (Figure 12b), clear grain size segregation is observed, concentrating smaller grains at the bottom.

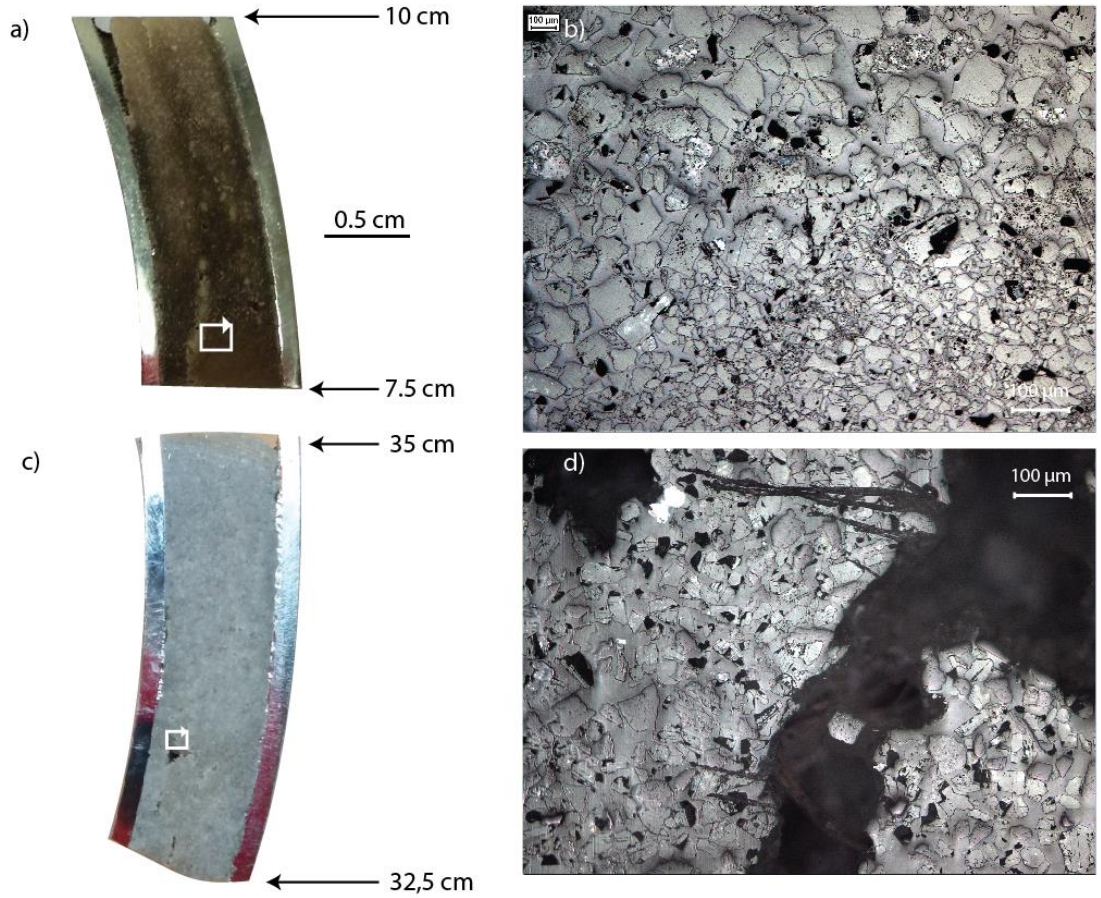

Figure 12 *a) Longitudinal cross-section of a steel segment 7.5-10cm downstream in Coil-A. b) Image showing different grain sizes and clear grain size segregation in Coil-A. c) Longitudinal cross-section of steel segment 32.5-35 cm downstream from Coil-B. d) Relatively uniform grain sizes in Coil-B. Black shapes are cavities formed due grain extraction during polishing. Flow direction is towards top of images.*

Secondary electron images show that the final material (Figure 13a) looks comparable to the starting material (Figure 5a), the grains show medium to high sphericity, though one might argue that the grain edges are less sharp (Figure 13b). As in the starting material, the surface of a single grain is smooth and also covered with fine grained material (Figure 13b). A magnified millimeter sized clump is displayed in Figure 13c and shows that it is surrounded by fine grained material (Figure 13d) which has accumulated in the pores of the coarser material (Figure 13c,d). Comparable features are observed in Coil-B (Figure 13e) which also shows fine grained material accumulation. Single grain analysis (anhydrite and K-Feldspar) shows no visible chemical alteration or new mineral formation (Figure 13g,f).

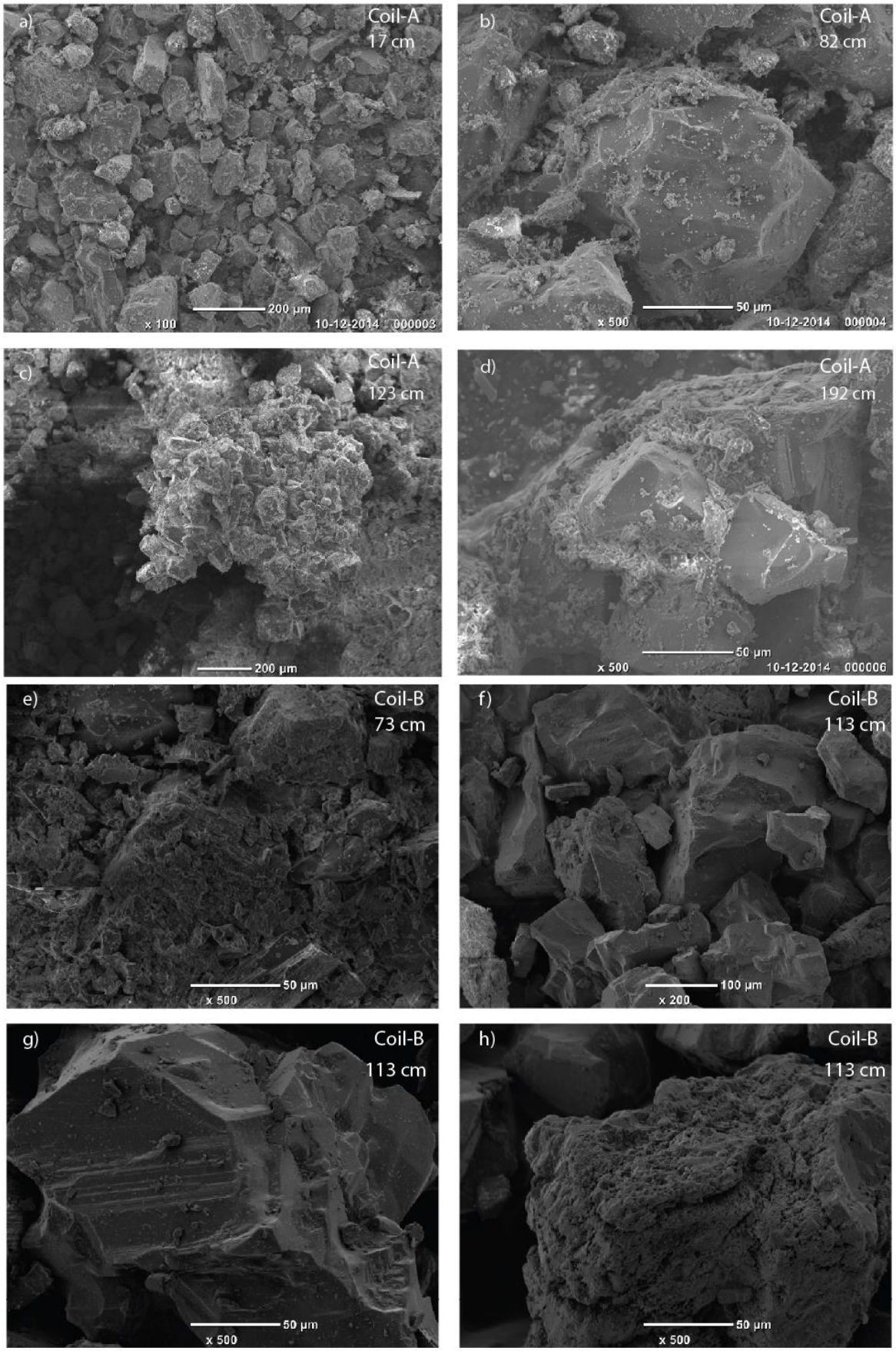

Figure 13 *Secondary electron images of material retrieved from Coil-A and Coil-B. Downstream distance is depicted top right. a) Shows an overview of the material as it was retrieved from Coil-A. b) Smoothed grain edges, surface area is covered with fine grained material. c) Clumped material. d) Fine grained material accumulated around larger grains. e) Accumulation of fine grained material and small chips, retrieved from Coil-B. b) Overview of anhydrite and feldspar grains. c) Close-up of a single anhydrite grain. d) Close-up of a single feldspar grain.*

3.3.4.2 Experiments performed using 0.5 M $NaHCO_3$ solution

Strong lithological differences were initially observed when removing material from the steel casing. In the first 5 cm segment of Coil-C, material was cohered to a single clump; little loose powder came with it and it had to be forcefully removed from the steel casing. 5 cm downstream and further downstream, material was partially cohered into white crescent shaped calcified crusts, which will be referred to as 'altered material', and was retrieved with higher amounts of loose powder (unaltered material). TGA analysis determined the calcite crusts consist of around 50 wt% carbonate, identified as calcite through XRD, whereas the incoherent powder from the same section contains 6 wt% carbonate and were only lightly attached to the steel casing. Cross sections taken at several intervals show white crescent shaped crusts in the left upper quarter and right quarter respectively (Figure 14e, f). Corresponding longitudinal sections (Figure 14a,b) show the altered material here is also seen to follow the steel-material interface, in a homogeneous way. In cross-sections and longitudinal sections from roughly halfway the meter-scale sample (106 cm downstream) and further we observe no chemical alteration (Figure 14c,d,g,h). Additionally, we did observe grainsize segregation phenomena in Coil-C, comparable to those previously described in Coil-A (Figure 12b). And we attribute the apparent differences at the top of each longitudinal section to be epoxy impregnation procedure artifacts, comparable to those seen in Figure 12a.

In addition, close-up reflected light images also show a clear distinction between the crescent shaped white material and the unaltered material (Figure 15a). Material from the crescent shape on the left side of the image (Figure 15b) shows hardly distinguishable grains and a lot of fine material. The left side of Figure 15a also shows little adherence of the altered material to the inside of the steel casing and forms a 0.5 mm wide aperture, such an aperture is rarely found though.

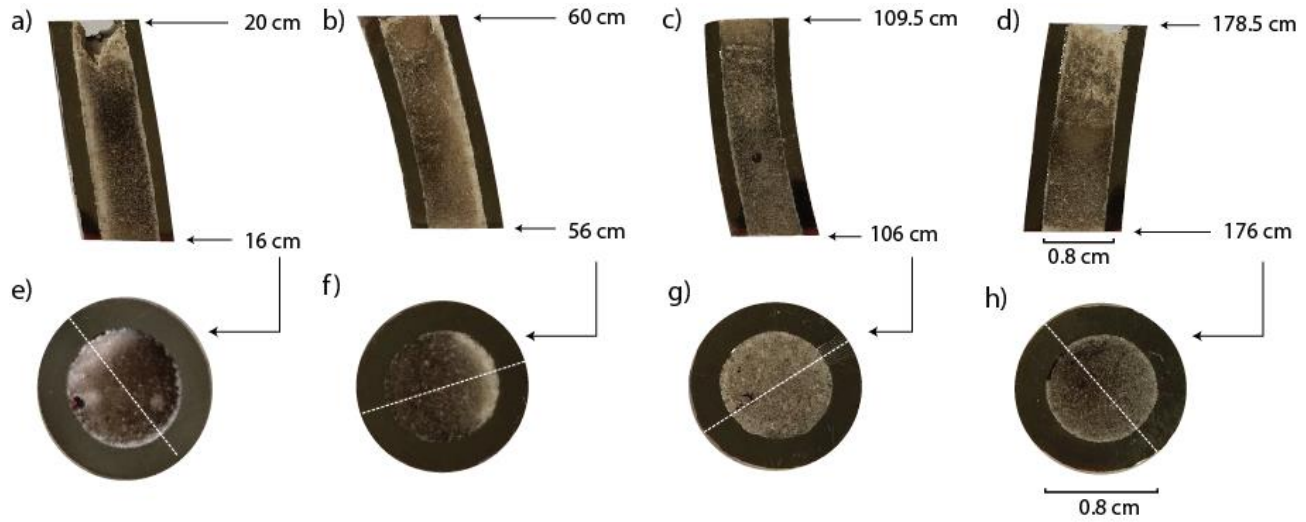

Figure 14 *Longitudinal-sections (a-d) and matching cross-sections (e-h) of Coil-C. Indicated lengths correspond with downstream location at which each section is taken. Orientation of the cross-sections correspond with actual orientation during experimentation, dashed lines correspond with the longitudinal section plane. Flow direction of each longitudinal section is upward; flow direction of each cross-section is towards viewer.*

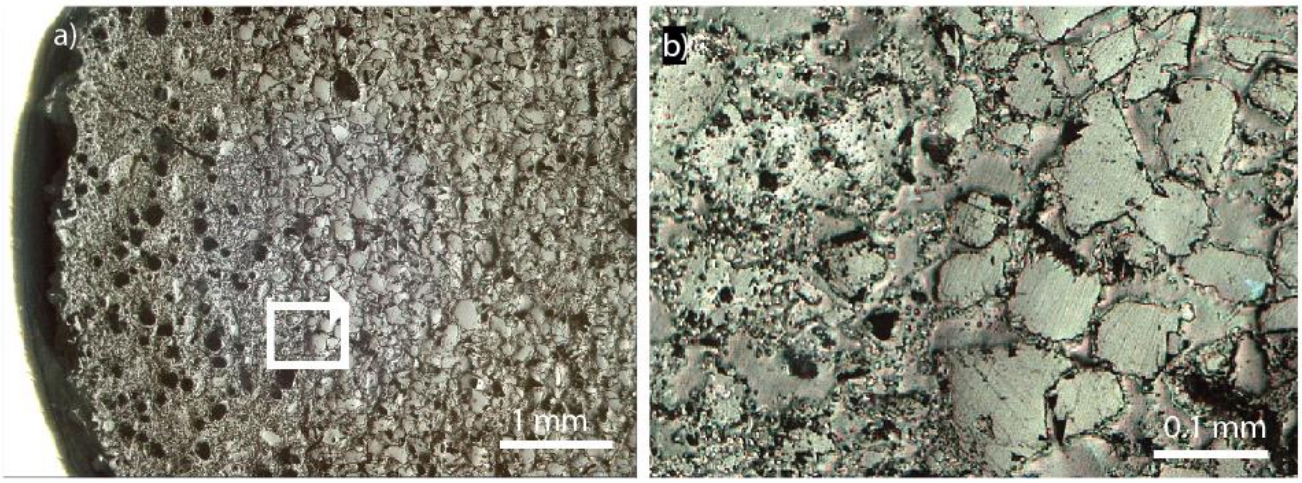

Figure 15 *Reflected light image of a cross section at 16 cm. a) Shows an overview of the crescent shaped material with unaltered powder. b) Zooms in on this image. Orientation of both images is rotated 45° counter clockwise with respect to Figure 14e.*

We carefully retrieved a mm thick calcite crust from around 17 cm downstream (Figure 16a-d). It presents the view on the altered-unaltered interface, of which Figure 15b is the cross sectional image (see Figure 11 for clarification). The loose powder is removed and the coherent material remains. An overview of the coherent grains is depicted in Figure 16a, in which no clear alterations with respect to the starting material can be observed. Grain sizes appear to be comparable, with sharp edges and a coating of dust. However, in contrast to the starting material, the single grains recovered from Coil-C are covered in small (10-20 µm) calcite crystals (Figure 16b), instead of dust. There are also dissolution pits and honeycomb dissolution structures visible on anhydrite grain surfaces, as is shown in Figure 16c,d. No other fine grained material is observed as was seen in the starting material (Figure 4) and other meter-scale samples (Figure 13b,g).

The steel-crust interface at 48 cm downstream, from a different mm sized calcite crust, is shown in Figure 16e-h, basically it represents the other side of the crust as depicted in Figure 16a-d. The overview image (Figure 16e) appears to show nearly all grains covered with calcite crystals. Upon closer inspection, many of these apperant grains are actually hollow skeletons completely made up of calcite crystals, which did not grow into the cavity (Figure 16f). However not all grains are hollow skeletons, some are intact, with a cover of calcite crystals (Figure 16g). Another close-up of the calcite crystals shows their trigonal crystal structure and relative uniform size (Figure 16h).

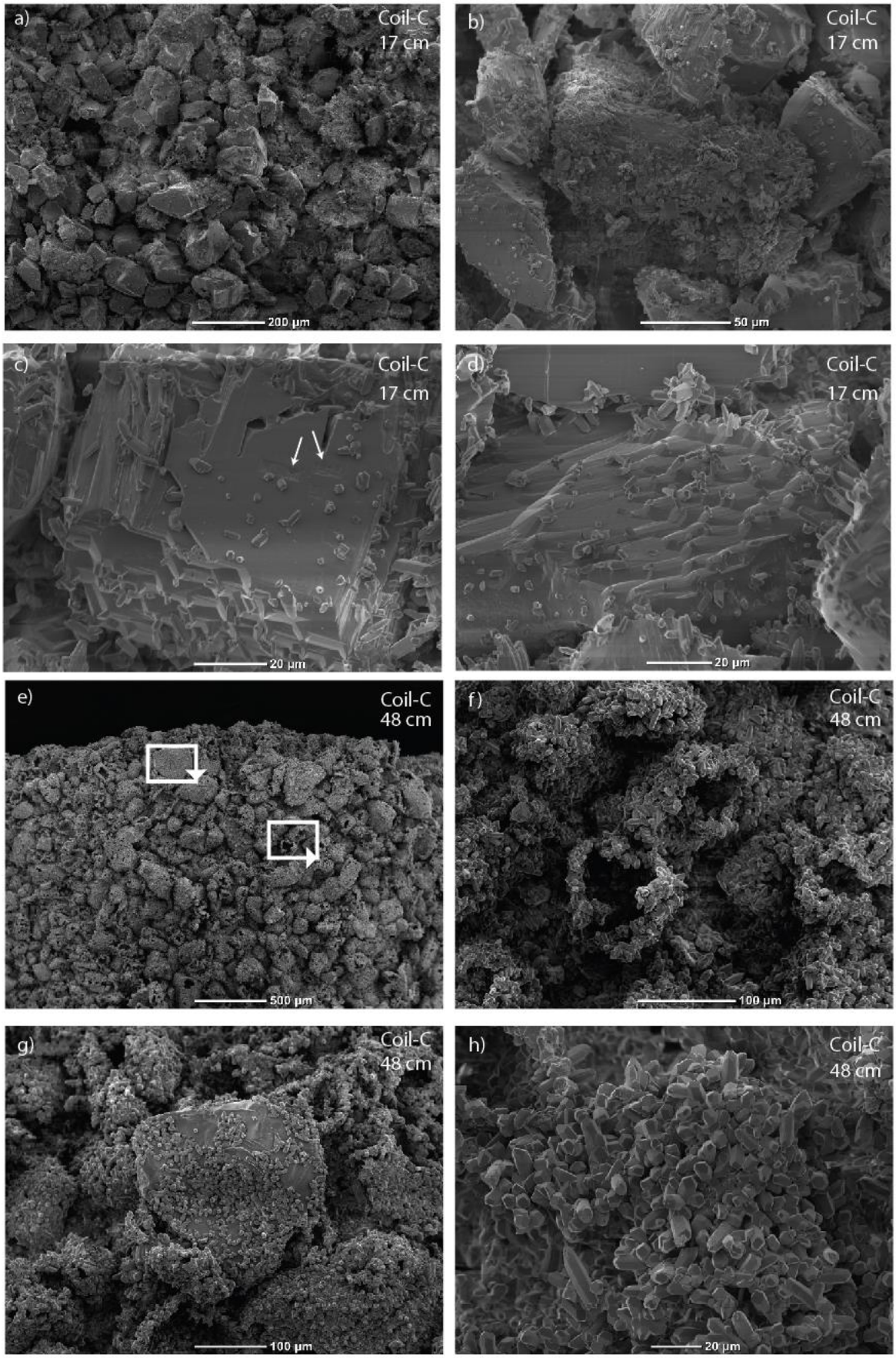

Figure 16 *Secondary electron images from around 17 cm (altered-unaltered interface) and 47 cm(steel-calcite crust interface) downstream into Coil-C. a) Overview image of the grains. b) Single grain covered in fine-grained material. c) Close-up of altered anhydrite grain with dissolution pits (arrows), honeycomb structures at the bottom, covered in calcite crystals. d) Honeycomb dissolution structures with calcite crystals.e) overview of cemented crusts. f) Hollow calcite crusts. g) Intact grain, covered with calcite crystals. h) Close-up of typical calcite crystals that form the calcite crusts.*

3.3.5 Permeability results

3.3.5.1 Experiments performed using CO_2-saturated water

Due to technical issues, the permeability data of Coil-A is inaccurate. The permeability data of Coil-B was measured after 17 and 28 days of reaction time. It was processed using the more accurate DPT data, and varied between $5.7x10^{-12}$ m2 and $5.9x10^{-12}$ m^2, i.e. all changes are below the measurement resolution of $<0.5x10^{-12}$ m^2 Due to the similarities in material and porosity it is assumed that the final and initial permeability measurements of Coil-B are comparable to those of Coil-A (Table 2).

3.3.5.2 Experiments performed using 0.5 M $NaHCO_3$ solution

By applying 0.2 MPa differential pressure, initial permeability was measured at $2.4x10^{-12}$ m^2 and final permeability at $4.5x10^{-12}$ m^2. In between flow-through was manifested at a flowrate of 10 ml/h, resulting in an applied pressure difference of <0.05MPa due to high sample permeability and consider this data indicative (Figure 17a). Data shows that for all, except the last flow-through run, permeability increases. Though there is no trend in the occurrence or duration of a shut-in event and the subsequent magnitude of permeability change. For example the second shut-in event results in a permeability increase of $0.1x10^{-12}$ m^2 over a shut-in duration of 3 days, while the fifth shut-in event results in permeability increase of $2.0x10^{-12}$ m^2 over a shut-in duration of 2 days. Furthermore it is notable that the last four flow-through runs result in flattening out of the permeability curve (Figure 17a). Complete permeability data of three 6h flow-through runs is displayed (Figure 17b), the data corresponds with the averaged permeability data points in Figure 17a. All three points show a relatively stable permeability over the course of a 6h run, compared to the permeability change that occurs during shut-in events. These flow-through runs are characteristic for all 9 flow-through runs.

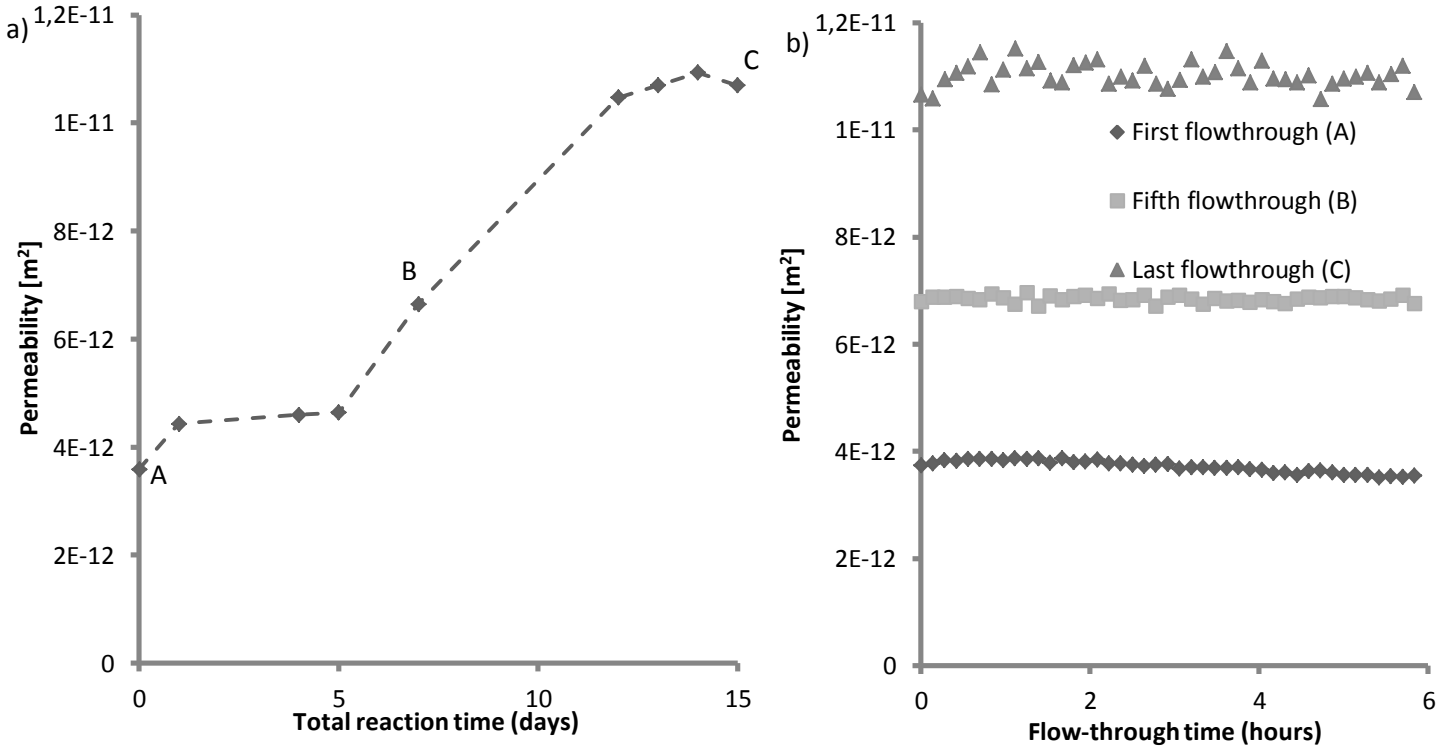

Figure 17 *a) Average permeability measurements vs total reaction time for Coil-C. In between each measurement point the sample was shut-in. b) Permeability data vs flow-through time for three given 6h runs. Letters (A,B,C) correspond with differential pressure data in a). Measurement points are set each 500 seconds.*

3.4 Geochemical modeling results

Here we show the geochemical modelling results on three end-member situations described in Pluymakers et al. (2014), by the use of Li and Duan (2011)'s model. Table 3 shows that heating the system, when still in contact with the atmosphere, results in precipitation of 0.86 g/l anhydrite, while small amounts ($2.2x10^{-3}$ g/l) $CaCO_3$ would dissolve. The effects of degassing the sample become clear by comparing heated and pressurized equilibrium conditions at 80 °C and 15.3 MPa with ambient equilibrium conditions (T = 20 °C, $_PCO_2$ = 0.1 MPa) showing a large increase in saturation concentrations of both CO_2 and $CaCO_3$. High $_pCO_2$ concentrations acidify the system and cause higher dissolved $CaCO_3$ concentrations, an increase of 1.62 g/l. Subsequent cooling and degassing of the system to ambient conditions will therefore result in the precipitation of equal amounts of $CaCO_3$, primarily caused by CO_2 degassing. Degassing and cooling the system will therefore result in the precipitation of approximately 0.005 gram of calcite from the 3 ml pore fluid in the sample used in the experiments.

	T = 20 °C, $_PCO_2$ = 0.1 MPa	T = 80 °C, $_PCO_2$ = 0.1 MPa	T = 80 °C, $_PCO_2$ = 15.3 MPa
$CaCO_3$ (g/l)	0.0025105	0.0047458	1.6453152
$CaSO_4$ (g/l)	2.0212297	1.1633299	0.6668137
CO_2 (g/l)	0.0004999	0.0004999	46.1256400

Table 3 *Saturation concentration of dissolved minerals for various P/T conditions (top row). After the quinary model of Li and Duan (2011).*

4. Discussion

In order to provide new data to test the viability of the anhydrite-calcite transformation reaction under storage conditions, and to gain insight into length-scale effects, we have performed batch reaction experiments and meter-scale flow-through experiments. XRD analysis of samples from the batch experiments, using CO_2-saturated water, shows calcite formation in samples that contained dolomite initially, while no calcite was detected if no dolomite was present initially. No change in carbonate content was observed using TGA. By contrast, XRD and TGA analysis of the batch experiments performed using alkaline fluids showed significant increases (5 wt%) in carbonate content.

Our meter-scale alkaline flow-through experiment, Coil-C, shows intense calcification structures far into the sample, combined with a two-fold permeability increase. In contrast, our performed flow-through experiments using CO_2-saturated water, show no calcite formation in the case of Coil-A, minor amounts in Coil-B, and no permeability changes. In the following, we will first compare the results of our batch reaction experiments with geochemical modelling results, and previous experimental and modelling work. We will attempt to explain the discrepancies noted and go on to discuss the permeability and microstructural results of our meter-scale flow-through experiments and their implications for fractured or faulted anhydrite systems. Lastly we will present some improvements to our experimental methodology, combining this with suggestions for further research.

4.1 Anhydrite to calcite transformation evaluated

4.1.1 Influence of degassing and initial carbonate content

In our CO_2-saturated fluid batch experiments (Batch 1, 2, 3), containing starting material with an initial 3-6 wt% dolomite content, we detected new calcite formation (XRD) (Table 1). However, no increase in total carbonate content was detected using TGA analysis. At the same time, our batch experiment using carbonate free anhydrite (Batch 5) showed no calcite formation using either analysis method. Microstructural analysis of single grains also showed no chemical alteration or new mineral formation (Figure 6a-d) and no other observable differences compared to the starting material (Fig. 5a-d). In addition, it is striking that in Coil-A, which we regard as a reactive flow-through experiment, no calcite was detected at any of the 8 measure points (Figure 7a). All our batch experiments were subjected to CO_2 degassing, while this effect was strongly reduced in our flow-through experiments, since these were flushed with deionized water prior to depressurization. This leads us to suspect that minor amounts of calcite formed in our batch experiments is related to CO_2 degassing. At high pCO_2, which is the case in our performed batch experiments, more CO_2 and H_2O react to form carbonic acid (H_2CO_3) (reaction (R1)). This controls the acidity of the system, which in turn is the controlling factor for the solubility of carbonate minerals (Garcia-Rios et al., 2014). Additionally, this is supported by our modelling results that show that a pCO_2 increase significantly enhances calcite solubility (Table 3). In nearly all of our starting material (anhydrite α, β, γ), initial amounts of carbonate are present in the form of dolomite. We argue that the calcite detected in our batch experiments is the result of enhanced dolomite dissolution, due to high pCO_2, which subsequently precipitated as calcite during the degassing phase. This viewpoint is also supported by our geochemical modelling (Table 3), which primarily shows that CO_2 degassing results in a decrease in dissolved calcite concentrations. In addition, this would explain why Batch 1, 2 & 3 show calcite formation using XRD, as there was an initial carbonate (dolomite) content present in the starting material. Furthermore, it also explains why TGA shows no increase in carbonate content in those experiments, as the overall carbonate content in the system remains constant. Additionally, one would expect that removing the initial carbonate content from the starting material prevents calcite formation, which is exactly the result of Batch 5 (Table 2). Likewise, reducing degassing effects, by replacing the CO_2 and carbonate saturated fluid with deionized water, should also inhibit calcite precipitation, as shown in our reactive flow-through experiment Coil-A. These findings indicate a) that the anhydrite-calcite transformation (reaction (R3)) is highly unlikely if just CO_2-saturated water and anhydrite are present in a system and b) that calcite formation occurs due to subsequent dolomite dissolution and precipitation.

Note here, that we assume that dolomite responds similarly to calcite when subjected to high pCO_2 and subsequent degassing. We are unsure why our XRD analysis does not detect any magnesite ($MgCO_3$), which is expected in comparable amounts if CO_2 degassing leads dissolved dolomite to precipitate. We have no answer to this paradox, so it requires further research.

4.1.2 Effects of an alkaline solution

Our batch experiments performed using anhydrite and alkaline solutions (0.16 M and 0.5 M $NaHCO_3$) all show significant amounts (3-6 wt%) of new calcite formation (Table 3). We do not have microstructural analysis of the batch experiments, but assume comparable microstructural alteration as seen with Coil-C (Figure 16a-g). Our K-feldspar enriched batch experiment (Batch 4) also indicates calcite formation (XRD), but no increase in total carbonate content (TGA) (Table 3). Since Batch 4 was subjected to degassing, we cannot rule out the cause of calcite formation. However, XRD analysis of our K-feldspar enriched meter-scale sample, Coil-B, showed calcite formation in several measured

sections (Figure 7b). As degassing effects were minimalized in this experiment, we attribute the calcite formation to K-feldspar acting as a weakly alkaline buffer.

4.1.3 Comments on previous work

Kuhn et al. (2009) argue that in order for reaction (R3) to occur, alkalinity or buffering capacity has to be present in a system and imply that just CO_2-saturated water will not react with anhydrite to form calcite, because an excess of acid (H^+) forms in reaction (R3). This inference is supported by geochemical modelling (Figure 1) which indicates a pH of at least 5.5 is required for reaction (R3) to be viable and confirmed this in performed batch experiments using $NaHCO_3$ and Na_2CO_3 solutions. Our results are consistent with their findings, as we have also shown alkalinity to be of utmost importance for calcite formation. Other experimental work on batch reactions, lasting up to 8 months, using CO_2-saturated fluids and anhydrite were conducted by Czernichowski-Lauriol et al. (1996) and Pearce et al. (1996). They reported the formation of 10 µm sized calcite crystals, and speculate that these were possibly formed due to a reaction between dissolved CO_2 and calcium ions, thus implying reaction (R3) to be viable at low-pH conditions. However, the anhydrite cores they experimented on are mentioned to contain mudstone lenses. No specification is given on the precise chemical composition of these lenses. However, it's not unlikely that these claystone/mudstone lenses contain mineralogical buffer capacity in the form silicate minerals (e.g. chlorite, kaolinite) (Beaucaire et al., 2004). And since alkalinity is a driving force for reaction (R3), plus given the long timescale (8 months) of reaction it is probable that this is the cause for observed calcite formation, as inferred for our experiments using K-Feldspar as a weakly alkaline source. Moreover, they do not describe their degassing procedure, which we have shown may cause calcite precipitation as well.

The most convincing case of the viability of reaction (R3) under acid conditions is described by Pluymakers et al. (2014). They report formation of 10 wt% calcite in two separate 1D compaction experiments using fluids saturated at ambient conditions to anhydrite α and subsequently pressurized with CO_2 at 15.3 MPa and 80°C. All grain fractions in those experiments were chemically analyzed before and after experimentation, ruling out that fractionation caused higher carbonate content. In addition, a control experiment using quartz instead of anhydrite α did not show any calcite formation. However, no microstructural evidence is presented. Using the quinary model of Li and Duan (2011) we show that 10 wt% calcite increase for the whole sample requires degassing of 3 liters of CO_2-saturated fluid saturated with respect to calciumcarbonate at 80°C and 15.3 MPa (Table 3). This volume is around two orders higher than the estimated pore volume in the experiments conducted by Pluymakers et al. (2014). Our calculations do show that a minor amount (0.005 g) of calcite will precipitate in the pore volume as a result of CO_2 degassing. Pluymakers et al. (2014) mention only small slivers were analyzed by TGA, instead of the whole 6.7 g sample. We regard it as a possibility that, during (slow) degassing, calcite precipitation may have concentrated at the surface of the sample, where analytical sampling likely occurred. If this is the location where small chips (<0.05 g) for TGA analysis were retrieved from, there is a possibility local carbonate content increase was measured. Relating the carbonate content increase to subsequent dolomite dissolution and calcite precipitation would explain why the control experiment using quartz did not show carbonate formation. Furthermore, our calculations show that the effects of heating and cooling the $CaSO_4$ saturated fluid are negligible (Table 3).

Our results are in agreement with those of Kuhn et al. (2009), implying that alkalinity is required in order for reaction (R3) to be viable. Furthermore we have offered a valid alternative explanation for the calcite formation reported by Czernichowski-Lauriol et al. (1996) and Pearce et al. (1996). Unfortunately we cannot fully explain the carbonate content increase reported by Pluymakers et al. (2014). In particular our experiments did not involve mechanical compaction, nor did our modelling methods. So we cannot exclude the potential effects compaction had on calcite formation. Because

the report by Pluymakers et al. (2014) is an isolated one, we remain skeptical regarding the possible relationship with anhydrite-calcite transformation. Instead, we suspect biasing in sampling of the reacted material, although more experiments are needed to substantiate this claim.

4.2 Meter-scale effects during flow-through of CO_2-saturated fluid

Unfortunately, no related research on meter scale samples has been found in the literature, so no comparison to previous research on length-scale can be made.

4.2.1 Sample preparation effects

Comparison between the meter-scale samples Coil-A and B did present us a good opportunity to assess the effects of sample preparation and initial heterogeneities dispersed over the entire sample length, because besides some possible dissolution features (Figure 13b) no other chemical alterations were observed. Particle size data from both samples shows a difference between the starting material (Figure 4) and material retrieved from Coil-A and B (Figure 10a and 10b). Data shows an increase in fine-grained material (<30µm), which is not observed in the starting material. Because of the similarities in chemical composition of the new fine grained material and the starting material, we assume it is not formed through chemical reaction. In addition, the lack of chemical alteration in Coil-A, also indicates that its complicated experimental history is of negligible relevance.

In reflected light images we have observed clear grain size segregation and less pore space in the fine grained section than in the coarser section (Figure 14b). No chemical alteration occurred in Coil-A, and only very minor amounts of calcite were formed in Coil-B. This, combined with the lack of trend in grain size reduction with position, and the formation of new fine-grained material (Figure 10a,b), implies that these changes in grain size are a result of sample preparation, i.e. tamping of the material. The effect of material tamping is thus apparently significant and should be taken into account when performing comparable research using experimental methods cf. section 2.3. It produces local porosity and local grain size anomalies, which could affect permeability and flow-paths. This is especially relevant for flow-through experiments that have a higher reactive potential, as reaction could concentrate in permeable or less permeable sections. We also suspect the clumpy material as retrieved from Coil-A and B (Figure 13c) and the fine grained accumulation (Figure 13d,f) to have formed, and be slightly coherent, due to material tamping and subsequent drying. In addition, we suspect the possible occurrence of apparent heterogeneities due to epoxy impregnation and saturation, as most longitudinal sections show similar differences when comparing the top of the section with the bottom (Figure 12a, 14a-d), as the top section is often lighter of color and separated from the steel casing.

4.2.2 K-Feldspar weathering, fluid analysis interpretation and permeability effects

In addition to our modelling results (Table 3), fluid analysis also shows enhanced carbonate dissolution due to CO_2 presence. Pure water samples from both experiments (Coil-A and B) show a close correlation in calcium and sulphate concentrations (Figure 9a,b). However, CO_2-saturated water samples show a large offset between sulphate and calcium concentrations. We explain this by the dissolution of dolomite due to high ${}_pCO_2$, which brings additional calcium and carbonate ions into solution (Figure 9b). Due to common-ion effect, less anhydrite is dissolved, as indicated by the reduced sulphate concentration, and more dolomite is in solution. This is also indicated by the increase in Mg^{2+} concentrations, which originate from dolomite. Coil-B shows higher amounts of dissolved dolomite, which is probably due to the longer reaction time (17 and 11 days), as Ca^{2+} concentrations are also slightly higher in general (Figure 9b).

Small concentrations of potassium ions (<10 ppm) are present in most fluid samples, which we interpret as a sampling artifact, most likely KOH remnants of the sampler fluid. Coil-B shows a significantly higher potassium concentration, while aluminum concentrations are nearly absent in all fluid samples (Figure 9b). This mismatch indicates a release of potassium with respect to aluminum. CO_2 flow-through experiments performed on anhydrite and feldspar containing cores (Shiraki and Dunn, 2000) indicate that the formation of kaolinite at those conditions is possible, at a relatively short timescale (167 h) and comparable conditions (80 C°, 16.6 MPa). However, that reaction does not favor potassium ion release. Because of the offset in potassium and aluminum concentration we interpret this offset as the transformation of K-feldspar into illite, which produces potassium ions, according to the following reaction

$$3KAlSi_3O_8 + 2CO_2(aq) + 2H_2O \leftrightarrow \text{muscovite (illite)} + 6SiO_2(aq) + 2K^+ + 2HCO_3^- \quad \text{(R4)}$$

Weathering reaction, forming illite, also shows how alkalinity in a system can form through the production of HCO_3^- ions. Feldspar dissolution is around 3-4 orders of magnitude slower than calcite and anhydrite reaction kinetics (Palandri and Kharaka, 2004), but these more sluggish reactions do affect reservoir pH and alkalinity and will be of importance in overall chemistry (Rosenqvist et al., 2014), indicating that feldspar weathering might be an important source for reservoir alkalinity. In addition, Kuhn et al. (2009) emphasize that the formation of a secondary silicate phase is of utmost importance for alkalinity formation. Additionally, Rochelle et al. (2004) mention there is reasonably good evidence that supports CO_2 enhanced feldspar weathering, followed by clay mineral precipitation and sometimes carbonate phases. On the other hand, other research done by Kaszuba and Janecky (2009) substantiate, that even though alkalinity is produced by reaction of carbonic acid with reservoir minerals, acidity produced by the dissolution of sc CO_2 cannot be compensated by the alkalinity of the in-situ brine, if the brine remains in place. However, our K-feldspar enriched flow-through experiment, Coil-B, does show minor amounts of calcite formation (Table 2, Figure 7b), which cannot be attributed to CO_2 degassing. Despite the slow reaction kinetics, we suspect that just enough calcite formed at 4/8 measurement points to exceed XRD detection limits (>0.25 wt%) due to the presence of K-feldspar. And we argue that, especially when given longer reaction time (months-years), a low alkaline source such as K-feldspar could be of importance.

We did not observe any permeability change in Coil-B, while according to our chemical data some calcite (XRD) and illite has formed. Secondary silica phase formation can cause permeability reduction as reported in Shiraki and Dunn (2000), where kaolinite pore neck precipitation is responsible for permeability decrease. We cannot however comment on possible effects both minerals have on the permeability, but we assume that formation was in such minor amounts that permeability was not affected.

4.3 Alkaline meter-scale flow-through effects

4.3.1. Microstructural and chemical interpretation

Alkaline fluid (0.5M $NaHCO_3$ solution) is shown to severely alter the simulated anhydrite fault gouge through the growth of calcite crystals (Figure 16h). This cohered the material and is more clearly seen at the steel-scale interface (Figure 16e) in which calcification is at a more advanced stage. We argue that the hollow calcite skeletons (Figure 16f), observed commonly in this interface (Figure 16e), are all remnants of anhydrite grains. An intermediate calcification development stage of the grains is seen in Figure 16c-d, which are partially covered in calcite and also partially dissolved. We suspect this would have eventually developed further into hollow calcite skeletons. The few grains that remain unaltered (Figure 16g) are interpreted as dolomite grains, which are unaffected by a $NaHCO_3$

solution compared to anhydrite grains (Figure 16c, d). Cross sections show that at least the first quarter of the meter-scale sample is partially calcified (Figure 14e,f). Assuming that the calcification correlates to chemical analyses, which quantifies calcite formation (Figure 8), it is evident that until around a position of 1/3 of the sample length significant calcification occurred. Beyond 1/3 of the sample length, the drop in calcite content is sharp and stabilizes at 1-2 wt% above the initial carbonate content (Figure 8). Possibly the alkaline fluid has lost much of its reactive potential at that point.

4.3.1.1 Porosity formation and retention

On the above basis, we assume that the shells made of calcite crystals are the skeletons of anhydrite grains. The anhydrite grains do not get replaced by calcite, but the initial pore space and partially dissolved grains get covered in a network of small calcite crystals. The anhydrite grain is eventually fully dissolved, creating secondary porosity as they are hollow. We have seen that grains partially get dissolved before they get fully covered by calcite crystals, so we assume the dissolved anhydrite grains are slightly smaller than the initial anhydrite grain size. In addition, the molar volume of calcite with respect to anhydrite is around 20% less. This way calcification of anhydrite gouge forms secondary porosity by building an interlocking network of hollow calcite skeletons. We have shown these calcite crystals to not form an impermeable barrier, also because apparently anhydrite dissolution continuous until a hollow shell remains. This eventually creates a zone existing solely out of porous calcite crust, containing little to no anhydrite anymore. We interpret this as the creation of a porous and permeable pathway for the alkaline fluid front, a pathway which is unaffected by alkalinity and vice versa.

4.3.1.2 Preferential flow-path development

The alteration zone of the material in Coil-C is described as a crescent shape (Figure 14e,f). This zoning indicates that the flow through the sample follows a preferred pathway; else more uniformly calcified cross-sections would be observed. All visible alteration occurs alongside the steel-powder interface (Figure 14a,b). We have reported that the first 5 cm segment of the meter-scale sample had to be forcefully removed from its casing and that it appeared to be entirely calcified, which is also supported by the chemical analysis, showing an average of 67 wt% carbonate.

We propose several reasons why this path formed at the steel-sample interface. First, the interface between the steel casing and anhydrite grains might be a natural more permeable path, due to the smooth surface of the steel casing on which the coarse and blocky grains are pushed on to. A second option is that this pathway is possibly formed due to the pore pressure increase, which caused the steel casing to expand. Thirdly, it is possible that tamping of the material, during preparation of the sample, caused local permeability changes, possibly compacting the center of the material more, causing flow to manifest at the edges. We have seen local porosity differences in unaltered samples (Figure 14b), which we attributed to sample preparation. It is foremost very likely that a combination of these factors is in play and affects the flow-path. We do not know how the flow-path is exactly located throughout the sample and whether it changes on the cm-scale, but within 40 cm a near 120° change in orientation is possible (compare Figure to 14e to 14f).

We interpret the calcified crescent shaped areas to be where the active flow passed through the sample, as those are the areas in which the anhydrite was transformed into calcite. We assume that the entire meter-scale sample is saturated with fluid, but apparently calcification does not occur homogeneously, but concentrates itself in these crescent shaped areas. We suspect that fresh alkaline fluid during flow-through does not reach into the unaltered sections that border the crescent shaped areas, and that the alkaline fluid flow concentrates in calcified areas. The calcified crescent shapes are made up of hollow calcite crusts, which appear to be completely deprived of any

anhydrite. Since no anhydrite is any longer present, alkaline fluid that passes through this calcified area will not lose reactive potential, as the alkaline fluid will not react with calcite and no anhydrite is present anymore for it to react with. We therefore suggest that a permeable calcite pathway is formed, which does not react with $NaHCO_3$ solution. The formation of this calcified pathway would allow alkaline fluid to flow through the meter-scale sample without losing reactive potential. We have no information of how the calcified zones exactly develop during flow-through or data which compares the permeability of a calcified area with that of unaltered powder, but apparently the calcified path is more permeable and does not seal. We therefore argue that the formation and development of the calcified pathway is a self- enhancing process. The initial pathway is formed due to sample heterogeneities, in which alkaline fluid flow-through concentrates. Through reaction with anhydrite, calcite is formed and eventually all anhydrite reacted away, leaving a permeable and unreactive path for more alkaline fluid. Through this we suspect a step-by-step downstream progradation of the calcified pathway up to near meter-scale.

4.3.2 Meter-scale alkaline sample permeability evaluation

As reported by Kuhn et al. (2009), who experimented on cm-scale anhydrite-cemented sandstone cores using 1M Na_2CO_3 solution, we also reported a permeability decrease. Though a slightly different chemical composition, $NaHCO_3$ is in this context comparable to Na_2CO_3, since it also has the capacity to react with anhydrite to form calcite. At an estimated 20% porosity of Kuhn et al. (2009) anhydrite-cemented cores and with a flowrate of 2 ml/h the residence time in their core is around 4 hours with a flow velocity of 1.5 cm/h. Our flow-through experiment used comparable residence time; however the flow velocity is around 50 cm/h. Permeability data from Kuhn et al. (2009) shows an initial permeability decrease, followed by a twofold increase. They flowed 3 L of solution through their sample. Our results resemble this data, as we also measured a near twofold permeability increase, $2.4x10^{-12}$ m^2 to $4.5x10^{-12}$ m^2. This implies that a 30 fold increase in flowrate and a 40 fold increase in sample length does not affect overall results, and that residence time is the key factor. Permeability data from the 10 ml/h flow-through runs show that up to the 6^{th} flow-through run at least, permeability constantly increases (Figure 17a). This is in contrast with high-alkaline flow-through experiments on anhydrite cemented sandstone cores (total anhydrite content 3 wt%) performed by Kazempour et al. (2012), who reported little change during flow-through and shut-in, using 1 wt% Na_2CO_3 solutions. They do not make any mention of why permeability remains constant, nor mention calcite formation. We suspect this might be due to the low anhydrite content (3 wt%) of the cores, through which the anhydrite-calcite 20% molar volume decrease has little effect on permeability.

For Coil-C, the only flow-through experiment with a readily available alkaline source, permeability approaches a near constant stage, at around $1.1x10^{-11}$ m^2 (Figure 17a) after 5 flow-through runs. Microstructural and chemical data also confirms that especially in the second meter of the sample, little chemical alteration took place, indicating potential for more calcification and more permeability increase. We therefore do not precisely know why the curve flattens out, but it might have to do with the low differential pressures we work with and that in order for the differential pressure transducer to record smaller pressure differences, the path through the sample has to become exponentially more permeable. So even though no permeability change is observed, we can assume permeability continues to increase, but we possibly need a more accurate differential pressure transducer in order to measure it.

Furthermore, it is curious that there is no clear relationship between shut-in time and the subsequent permeability increase, even though it is shown that most permeability change occurs during shut-ins, and practically none during flow-through (Figure 17b), as all flow-through runs show no significant change in permeability (compared to change during shut-in events) with flow-through time. However, from our microstructural and chemical data we suspect that most reaction and

microstructural change (e.g. anhydrite dissolution, calcite precipitation) occurred during the 6h flow-through events, as the intense calcified structures fade out at around 70 cm into Coil-C, indicating loss of reactive potential of the alkaline fluid. If most reaction occurred during shut-in events, calcification would have been expected to have dispersed more equally throughout the entire 2 m of sample length. We don't have an answer to this contradiction, and to answer this more research would be needed. For example similar flow-through experiments, but at other flowrates or a continuous flow-through experiment, to assess better the effects of shut-in and flowthrough.

4.4 Implications for fault systems in anhydrite formations in nature

In our experiments we have found no evidence that supports the possible reaction of anhydrite with CO_2-saturated water into calcite, without an alkaline source present. We therefore infer that faulted or fractured anhydrite caprock, which is exposed to CO_2-saturated water, has no risk of calcite formation and therefore no porosity or permeability alterations, without mechanical compaction present. However, we cannot fully refute the doubts expressed in Pluymakers et al. (2014) regarding this matter, as have no solid explanation for the carbonate increase seen in their compaction experiments. These conclusions also hold for faults in CO_2 rich anhydrite-bearing seismic terranes (e.g. Apennines).

In contrast, flow-through of alkaline fluid through simulated anhydrite fault gouge shows severe chemical alteration, causing formation and retainment of porosity and a permeable calcified pathway. These calcite crusts average at around 50 wt% calcite, but possibly consisting of more than 90 wt% calcite further towards the steel-calcite crust interface, as shown by our microstructural analysis (Figure 16e,f). The penetration of a high alkalinity fluid into faulted anhydrite would result in strong calcification of the anhydrite fault gouge. Carbonate fault gouge shows strong velocity-weakening frictional behavior at reservoir conditions (Verberne et al., 2014), so material transformation into small calcite grains may severely affect geomechanic fault properties, especially since calcite formation is concentrated in a zone. In addition, alkaline fluids promote secondary porosity formation, as we have seen anhydrite grains get fully dissolved and replaced by a calcite network (Figure 16e-h), possibly enhancing formation fluid outflow. In our 2 meter long sample we have seen a near 70 cm penetration of intense calcification and permeability increase, in fewer than 60 h of flow-through, with minor increase in calcite content over the remaining meter-scale section. This infers that caution has to be applied when anhydrite capped reservoirs are injected with alkaline fluids (e.g. employing fly ash) combined with CO_2, which could occur for example through a combination of industrial alkaline waste disposal with CCS (Bobicki et al., 2012). Similar caution applies to injection of alkaline fluids (e.g. $NaHCO_3$, Na_2CO_3) that directly promote calcite formation from anhydrite, used in the light or EOR, for example (Lorenz and Peru, 1989).

Degassing effects in our experiments were not significant, though do indicate a potential for carbonate mass transfer. As our modeling results indicate high pCO_2 fluids, saturated with respect to calcite, have large degassing and calcite precipitation potential (Table 3). If such a fluid would degas in a fault, calcite would precipitate and possibly alter the fault properties. However, due to mass transfer, permeability decrease and fault sealing could perhaps be observed.

4.5 Suggestions for further research

4.5.1 Methodological improvements

During our experimental work we noticed several possible improvements to our methodology. In order to achieve a higher grade of initial porosity we firmly tamped the material after pouring it in the steel casing. Tamping however, evidently breaks grains into smaller fractions and forms very fine

material (Figure 10a,b, 12a), possibly leading to permeability and porosity heterogeneities. The question is whether this outweighs the advantage of an overall initial lower porosity, or perhaps it is better to find a more gentle way to provide some initial tamping. In addition, if doing a permeability analysis on powdered material in long-scale samples such as ours, we advise to make use of pumps with a larger volume. Since some conflict exists between permeability data and microstructural data to whether most reaction occurs during or after experimentation, we are interested to see continuous permeability data. Due to the high sample permeability, our Teledyne ISCO Model 65D pumps emptied in around 6 hours. The use of pumps with larger volumes, or lower permeability sample material, would allow for a more continuous experiment that could continue running during the night and over the weekends. The use of a high alkaline fluid has proven to be very reactive, especially in the beginning of the meter-scale sample (Figure 8). To more accurately assess these effects, we advise a narrower sample scale and use 1-2 cm intervals to make steel sections, instead of 5 cm. Through this method also an accurate meter-scale flow-path description can be formed.

4.5.2 Further work on the anhydrite-calcite transformation

Besides the intriguing case of Pluymakers et al. (2014), little evidence remains regarding the anhydrite-calcite transformation, under acid conditions. We were able to provide some hypotheses to where the apparent calcite content increase originated from, but we cannot draw definite conclusions. Therefore, we suggest that in order to reevaluate the 10 wt% increase in calcite content, a new set of identical 1D compaction experiments could be run. Since CO_2 degassing is involved in those experiments and initial carbonate content is present, a mass transfer of carbonates can occur. Therefore, these experiments have to be carried out using pure or acid-treated anhydrite powder, in such a way that no carbonates (and preferably no other impurities) remain in the starting material. As in one of our experiments (Batch 4), this provides to opportunity to purely study the effects of anhydrite. In a way these experiments can be regarded as the definite control experiments to Pluymakers et al. (2014). Furthermore, the absence of initial carbonate content would also present the opportunity to use TGA as a very accurate method to detect small quantities of calcite formation. In addition, some month to yearlong batch experiments containing similar acid-treated anhydrite could be run. Ideally the effect of degassing should be absent as well, but we suspect that if no initial carbonates are present, degassing effects will be insignificant.

4.5.3 Other suggestions

In our experiments we lack the effect of confining pressure. In fault systems confining pressure causes processes that lead to fault healing and sealing and express a dominating aspect over the overall behavior of the fault. In that light it is not only interesting, but foremost necessary to apply a confining pressure in order to actually draw more definite conclusions about the effects of alkaline fluid on an anhydrite fault and the porous calcite network, as formed in our experiments. Furthermore, we cannot fully exclude that the carbonate content increase Pluymakers et al. (2014) could possibly be related to the effect of compaction.

In Coil-C we make use of relatively high alkaline fluid (0.5 M $NaHCO_3$ solution). However, what the effect of slightly (in-situ) alkaline formation fluids on anhydrite fault gouge would be, is not investigated, and is a very relevant natural analogue. First, there is a lack of complete chemical analyses that quantify minor buffer species in a formation fluid (Bachu et al., 2003), so there is little known about low alkaline formations. However, we do mention several accounts of alkalinity formed due to CO_2 enhanced feldspar weathering and subsequent secondary silica phase and carbonate precipitation (section 4.2.2). At the moment we cannot infer how anhydrite fault rock would respond to low alkalinity formation fluids that either formed naturally or due to CO_2- K-feldspar reactions (reaction (R4)). It is possible, that given more time and flow-through volume, in an experiment using

low alkaline fluids, chemical and microstructural alterations will be comparable to those seen in high alkalinity flow-through experiments.

Finally, there remains a large potential for meter-scale experiments in general. Not only more long-scale experiments regarding alkaline fluid and degassing are among the possibilities, but since scale in general is an issue, many potential scenarios containing granular material could profit from long-scale research conform our methodology.

5. Conclusions

Batch and meter-scale flow-through experiments have been performed on simulated anhydrite fault gouge using CO_2-saturated water and $NaHCO_3$ solutions at typical reservoir conditions of 10.0 MPa and at 80°C. We conducted batch experiments to provide a clear consensus on to what extent acidic CO_2-saturated water influences the transformation of anhydrite into calcite, and whether buffer capacity is a requirement for this reaction. Additionally, we performed some geochemical modelling under similar conditions and combined these results with our experimental results to comment on previous work regarding the anhydrite-calcite transformation. Furthermore, we conducted the set of meter-scale flow-through experiments to assess any possible length-scale effects related to the anhydrite-calcite transformation. These conclusions are directly relevant to understanding of fluid transport along anhydrite bearing fault systems in CO_2 rich environments. Our main findings are as follows:

I. Buffer capacity is of utmost importance to transform anhydrite into calcite, acidic CO_2-saturated (pH = 3-4) water does not react with anhydrite into calcite. Therefore there is no risk of calcite formation or permeability change due to CO_2-saturated water penetrating faulted or fractured anhydrite caprock.
II. We call for caution when injecting high alkaline fluids into anhydrite capped reservoirs, for example through a combination of alkaline waste disposal/alkaline EOR combined with CCS, as we show that flow-through of 540 ml 0.5 M $NaHCO_3$ solution causes formation of zoned mm-thick calcite crusts on near meter-lengthscale in under 60h of flowtime. Formation of a localized calcite zone in a fault system may severely affect transport and geomechanical fault properties.
III. In the meter-scale alkaline flow-through experiment (Coil-C) we measured permeability increase after every shut-in event, adding up to a two-fold permeability increase. During actual flow-through no permeability change was observed. This data is in accordance with previous cm-scale experiments and also demonstrates that the 20% porosity increase associated with the anhydrite-calcite transformation also results in permeability increase.
IV. Minor amounts of calcite detected in (up to 2 month long) acid batch experiments are formed due to high pCO_2 conditions, which cause dolomite dissolution followed by carbonate re-precipitation due to CO_2 degassing. No calcite is formed in batch experiments containing CO_2-saturated water and carbonate-free anhydrite. These findings help explain minor calcite formation mentioned in previous work regarding the anhydrite-calcite transformation.
V. Calcite crust formation, through the reaction of anhydrite with alkaline 0.5M $NaHCO_3$ solution in the flow-through experiment, occurs through the envelopment of already partially dissolved anhydrite grains, by 10-20 µm sized calcite crystals. Subsequently, the remaining anhydrite grain gets further dissolved, leaving a zoned interlocking porous network of calcite skeletons, concentrated at the steel casing-anhydrite gouge interface. This forms an unreactive flow-path for alkaline fluid, increasing length-scale penetration of this calcified pathway through a self-enhancing process.

VI. Tamping simulated anhydrite fault gouge after insertion into the steel casing causes grain fracturing, local porosity and permeability differences, and increase in fine-grained material. We doubt the necessity of tamping, which could prevent these methodology artifacts, as it is observable through microstructural and grain size analyses, and should not be neglected in similar experiments.

VII. We express the need for further research through the addition of confining pressure during similar flow-through experiments. This should provide more realistic insights regarding calcite formation and pathway development in meter-scale experiments. We also suggest a set of experiments, using carbonate-free anhydrite, which should give more insight in the origin of increase in calcite content reported in previous experiments performed by Pluymakers et al. (2014).

Acknowledgements

This MSc thesis was written in collaboration with the HPT-Lab at Utrecht University. We foremost would like to thank Tim Wolterbeek, and Anne Pluymakers for their valuable assistance, ideas, discussions and elaborate feedback, you have been of great help and guided us through this research. We also thank prof. dr. Chris Spiers and dr. Colin Peach for their help and offering the opportunity to conduct this research in the HPT Lab. We too thank Gert Kastelein and Peter van Krieken for their valuable technical assistance with the experimental set-up and post-experimental analysis.

References

Armitage, P., Faulkner, D., and Worden, R., 2013, Caprock corrosion: Nature Geoscience, v. 6, no. 2, p. 79-80.

Bachu, S., 2000, Sequestration of CO2 in geological media: criteria and approach for site selection in response to climate change: Energy Conversion and Management, v. 41, no. 9, p. 953-970.

Bachu, S., Michael, K., and Adams, J., Effects of In Situ Conditions on Aquifer Capacity for CO2 Sequestration in Solution, *in* Proceedings Proceedings of Second National Conference on Carbon Sequestration2003, p. 5-8.

Beaucaire, C., Pearson, F., and Gautschi, A., 2004, Chemical buffering capacity of clay rock: Stability and buffering capacity of the geosphere for long-term isolation of radioactive waste, p. 147.

Bobicki, E. R., Liu, Q., Xu, Z., and Zeng, H., 2012, Carbon capture and storage using alkaline industrial wastes: Progress in Energy and Combustion Science, v. 38, no. 2, p. 302-320.

Brzesowsky, R., Spiers, C., Peach, C., and Hangx, S., 2011, Failure behavior of single sand grains: Theory versus experiment: Journal of Geophysical Research: Solid Earth (1978–2012), v. 116, no. B6.

Charola, A. E., Pühringer, J., and Steiger, M., 2007, Gypsum: a review of its role in the deterioration of building materials: Environmental Geology, v. 52, no. 2, p. 339-352.

Collettini, C., De Paola, N., and Faulkner, D., 2009, Insights on the geometry and mechanics of the Umbria–Marche earthquakes (Central Italy) from the integration of field and laboratory data: Tectonophysics, v. 476, no. 1, p. 99-109.

Czernichowski-Lauriol, I., Sanjuan, B., Rochelle, C., Bateman, K., Pearce, J., and Blackwell, P., 1996, Analysis of the geochemical aspects of the underground disposal of CO2, Academic Press, Deep Injection Disposal of Hazardous and Industrial Waste.

De Paola, N., Collettini, C., Faulkner, D., and Trippetta, F., 2008, Fault zone architecture and deformation processes within evaporitic rocks in the upper crust: Tectonics, v. 27, no. 4.

Garcia-Rios, M., Cama, J., Luquot, L., and Soler, J. M., 2014, Interaction between CO 2-rich sulfate solutions and carbonate reservoir rocks from atmospheric to supercritical CO 2 conditions: Experiments and modeling: Chemical Geology, v. 383, p. 107-122.

Geluk, M., 2007, Permian: Geology of the Netherlands. Royal Netherlands Academy of Arts and Sciences, p. 63-83.

Johnson, J. W., Nitao, J. J., and Knauss, K. G., 2004, Reactive transport modeling of CO2 storage in saline aquifers to elucidate fundamental processes, trapping mechanisms and sequestration partitioning: Geological storage of carbon dioxide, v. 233, p. 107-128.

Kaszuba, J. P., and Janecky, D. R., 2009, Geochemical impacts of sequestering carbon dioxide in brine formations: Carbon Sequestration and its Role in the Global Carbon Cycle, p. 239-247.

Kazempour, M., Sundstrom, E., and Alvarado, V., 2012, Geochemical modeling and experimental evaluation of high-pH floods: Impact of Water–Rock interactions in sandstone: Fuel, v. 92, no. 1, p. 216-230.

King, M., Mubarak, A., Kim, J., and Bott, T., 1992, The mutual solubilities of water with supercritical and liquid carbon dioxides: The Journal of Supercritical Fluids, v. 5, no. 4, p. 296-302.

Kuhn, M., Clauser, C., Vosbeck, K., Stanjek, H., Meyn, V., Back, M., and Peiffer, S., 2009, Mineral trapping of CO2 in operated hydrogeothermal reservoirs: AAPG Studies in Geology, v. 59, p. 545-552.

Li, J., and Duan, Z., 2011, A thermodynamic model for the prediction of phase equilibria and speciation in the H2O–CO2–NaCl–CaCO3–CaSO4 system from 0 to 250 °C, 1 to 1000 bar with NaCl concentrations up to halite saturation: Geochimica et Cosmochimica Acta, v. 75, no. 15, p. 4351-4376.

Li, S., Dong, M., Li, Z., Huang, S., Qing, H., and Nickel, E., 2005, Gas breakthrough pressure for hydrocarbon reservoir seal rocks: implications for the security of long-term CO2 storage in the Weyburn field: Geofluids, v. 5, no. 4, p. 326-334.

Lorenz, P., and Peru, D., 1989, Guidelines help select reservoirs for NaHCO3 EOR: Oil and Gas Journal;(USA), v. 87, no. 37.

Luquot, L., and Gouze, P., 2009, Experimental determination of porosity and permeability changes induced by injection of CO2 into carbonate rocks: Chemical Geology, v. 265, no. 1–2, p. 148-159.

Mao, S., and Duan, Z., 2009, The viscosity of aqueous alkali-chloride solutions up to 623 K, 1,000 bar, and high ionic strength: International Journal of Thermophysics, v. 30, no. 5, p. 1510-1523.

Palandri, J. L., and Kharaka, Y. K., 2004, A compilation of rate parameters of water-mineral interaction kinetics for application to geochemical modeling: DTIC Document.

Pearce, J. M., Holloway, S., Wacker, H., Nelis, M. K., Rochelle, C., and Bateman, K., 1996, Natural occurrences as analogues for the geological disposal of carbon dioxide: Energy Conversion and Management, v. 37, no. 6–8, p. 1123-1128.

Pluymakers, A. M., Peach, C. J., and Spiers, C. J., 2014, Diagenetic compaction experiments on simulated anhydrite fault gouge under static conditions: Journal of Geophysical Research: Solid Earth.

Rochelle, C., Czernichowski-Lauriol, I., and Milodowski, A., 2004, The impact of chemical reactions on CO2 storage in geological formations: a brief review: Geological Society, London, Special Publications, v. 233, no. 1, p. 87-106.

Rochelle, C., Pearce, J., and Holloway, S., 1999, The underground sequestration of carbon dioxide: containment by chemical reactions in the deep geosphere: Geological Society, London, Special Publications, v. 157, no. 1, p. 117-129.

Rosenqvist, J., Kilpatrick, A. D., Yardley, B. W., and Rochelle, C. A., Dissolution of K-feldspar at CO2-saturated conditions, *in* Proceedings EGU General Assembly Conference Abstracts2014, Volume 16, p. 10909.

Scott, V., Gilfillan, S., Markusson, N., Chalmers, H., and Haszeldine, R. S., 2013, Last chance for carbon capture and storage: Nature Clim. Change, v. 3, no. 2, p. 105-111.

Shiraki, R., and Dunn, T. L., 2000, Experimental study on water–rock interactions during CO2 flooding in the Tensleep Formation, Wyoming, USA: Applied Geochemistry, v. 15, no. 3, p. 265-279.

van der Meer, L., and van Wees, J.-D., Limitations to storage pressure in finite saline aquifers and the effect of CO2 solubility on storage pressure, *in* Proceedings SPE Annual Technical Conference and Exhibition2006, Society of Petroleum Engineers.

Verberne, B., Spiers, C., Niemeijer, A., De Bresser, J., De Winter, D., and Plümper, O., 2014, Frictional properties and microstructure of calcite-rich fault gouges sheared at sub-seismic sliding velocities: Pure and Applied Geophysics, v. 171, no. 10, p. 2617-2640.